EUROPEAN ORGANIZATION FOR NUCLEAR RESEARCH

CERN–PPE/94–121

22 July 1994

A Study of Radiative Muon-Pair Events at Z^0 Energies and limits on an additional Z' Gauge Boson

DELPHI Collaboration

Abstract

An analysis is reported on the channel $e^+e^- \to \mu^+\mu^-(n\gamma)$, n=1,2.., using data taken with the DELPHI detector at LEP from 1990 to 1992. Differential cross sections of the radiative photons as a function of photon energy and of the angle between the photon and the muon are presented. No significant deviations from expectations are observed.
The data are also used to extract the muon-pair cross section and asymmetry below the Z^0 peak by using those events with relatively hard initial state radiative photon(s). The measured cross section and asymmetry show no significant deviation from the Standard Model expectations.
These results together with the DELPHI cross section and asymmetry measurements at the LEP energies from the 1990 to 1992 running periods are used to determine limits on the Z^0-Z' gauge boson mixing angle $\theta_{Z'}$ and on the Z' mass. There is no indication of the existence of a Z'; the limits obtained on the mixing angle substantially improve upon existing limits. The 95% confidence level allowed ranges of $\theta_{Z'}$ in various models are:

$$
\begin{array}{lll}
-0.0070 \leq \theta_{Z'} \leq 0.0078, & & E_6(\chi) \text{ model,} \\
-0.0075 \leq \theta_{Z'} \leq 0.0095, & & E_6(\psi) \text{ model,} \\
-0.029 \leq \theta_{Z'} \leq 0.029, & & E_6(\eta) \text{ model,} \\
-0.0068 \leq \theta_{Z'} \leq 0.0082, & & \text{L-R}(1.) \text{ model,} \\
-0.0057 \leq \theta_{Z'} \leq 0.0077, & & \text{L-R}(\sqrt{2}) \text{ model.}
\end{array}
$$

(Submitted to Zeit. f. Physik C)

P.Abreu[20], W.Adam[7], T.Adye[37], E.Agasi[30], I.Ajinenko[42], R.Aleksan[39], G.D.Alekseev[14], P.P.Allport[21], S.Almehed[23], F.M.L.Almeida[47], S.J.Alvsvaag[4], U.Amaldi[7], A.Andreazza[27], P.Antilogus[24], W-D.Apel[15], R.J.Apsimon[37], Y.Arnoud[39], B.Åsman[44], J-E.Augustin[18], A.Augustinus[30], P.Baillon[7], P.Bambade[18], F.Barao[20], R.Barate[12], D.Y.Bardin[14], G.J.Barker[34], A.Baroncelli[40], O.Barring[7], J.A.Barrio[25], W.Bartl[50], M.J.Bates[37], M.Battaglia[13], M.Baubillier[22], J.Baudot[39], K-H.Becks[52], M.Begalli[36], P.Beilliere[6], P.Beltran[9], A.C.Benvenuti[5], M.Berggren[41], D.Bertrand[2], F.Bianchi[45], M.Bigi[45], M.S.Bilenky[14], P.Billoir[22], J.Bjarne[23], D.Bloch[8], J.Blocki[51], S.Blyth[34], V.Bocci[38], P.N.Bogolubov[14], T.Bolognese[39], M.Bonesini[27], W.Bonivento[27], P.S.L.Booth[21], G.Borisov[42], C.Bosio[40], B.Bostjancic[43], S.Bosworth[34], O.Botner[48], E.Boudinov[42], B.Bouquet[18], C.Bourdarios[18], T.J.V.Bowcock[21], M.Bozzo[11], S.Braibant[2], P.Branchini[40], K.D.Brand[35], R.A.Brenner[13], H.Briand[22], C.Bricman[2], L.Brillault[22], R.C.A.Brown[7], J-M.Brunet[6], L.Bugge[32], T.Buran[32], A.Buys[7], J.A.M.A.Buytaert[7], M.Caccia[27], M.Calvi[27], A.J.Camacho Rozas[41], R.Campion[21], T.Camporesi[7], V.Canale[38], K.Cankocak[44], F.Cao[2], F.Carena[7], P.Carrilho[47], L.Carroll[21], R.Cases[49], C.Caso[11], M.V.Castillo Gimenez[49], A.Cattai[7], F.R.Cavallo[5], L.Cerrito[38], V.Chabaud[7], A.Chan[1], M.Chapkin[42], Ph.Charpentier[7], L.Chaussard[24], J.Chauveau[22], P.Checchia[35], G.A.Chelkov[14], P.Chliapnikov[42], V.Chorowicz[22], J.T.M.Chrin[49], V.Cindro[43], P.Collins[34], J.L.Contreras[18], R.Contri[11], E.Cortina[49], G.Cosme[18], G.Cosmo[46], C.Cossutti[46], F.Couchot[18], H.B.Crawley[1], D.Crennell[37], G.Crosetti[11], J.Cuevas Maestro[33], S.Czellar[13], E.Dahl-Jensen[28], J.Dahm[52], B.Dalmagne[18], M.Dam[32], G.Damgaard[28], E.Daubie[2], A.Daum[15], P.D.Dauncey[37], M.Davenport[7], J.Davies[21], W.Da Silva[22], C.Defoix[6], P.Delpierre[26], N.Demaria[34], A.De Angelis[7], H.De Boeck[2], W.De Boer[15], S.De Brabandere[2], C.De Clercq[2], M.D.M.De Fez Laso[49], C.De La Vaissiere[22], B.De Lotto[46], A.De Min[27], L.De Paula[47], C.De Saint-Jean[39], H.Dijkstra[7], L.Di Ciaccio[38], F.Djama[8], J.Dolbeau[6], M.Donszelmann[7], K.Doroba[51], M.Dracos[8], J.Drees[52], M.Dris[31], Y.Dufour[7], F.Dupont[12], D.Edsall[1], R.Ehret[15], T.Ekelof[48], G.Ekspong[44], M.Elsing[52], J-P.Engel[8], N.Ershaidat[22], M.Espirito Santo[20], D.Fassouliotis[31], M.Feindt[7], A.Fenyuk[42], A.Ferrer[49], T.A.Filippas[31], A.Firestone[1], H.Foeth[7], E.Fokitis[31], F.Fontanelli[11], F.Formenti[7], J-L.Fousset[26], B.Franek[37], P.Frenkiel[6], D.C.Fries[15], A.G.Frodesen[4], R.Fruhwirth[50], F.Fulda-Quenzer[18], H.Furstenau[7], J.Fuster[7], D.Gamba[45], M.Gandelman[17], C.Garcia[49], J.Garcia[41], C.Gaspar[7], U.Gasparini[35], Ph.Gavillet[7], E.N.Gazis[31], D.Gele[8], J-P.Gerber[8], P.Giacomelli[7], D.Gillespie[7], R.Gokieli[51], B.Golob[43], V.M.Golovatyuk[14], J.J.Gomez Y Cadenas[7], G.Gopal[37], L.Gorn[1], M.Gorski[51], V.Gracco[11], F.Grard[2], E.Graziani[40], G.Grosdidier[18], P.Gunnarsson[44], J.Guy[37], U.Haedinger[15], F.Hahn[52], M.Hahn[44], S.Hahn[52], S.Haider[30], Z.Hajduk[16], A.Hakansson[23], A.Hallgren[48], K.Hamacher[52], W.Hao[30], F.J.Harris[34], V.Hedberg[23], R.Henriques[20], J.J.Hernandez[49], J.A.Hernando[49], P.Herquet[2], H.Herr[7], T.L.Hessing[21], E.Higon[49], H.J.Hilke[7], T.S.Hill[1], S-O.Holmgren[44], P.J.Holt[34], D.Holthuizen[30], P.F.Honore[6], M.Houlden[21], J.Hrubec[50], K.Huet[2], K.Hultqvist[44], P.Ioannou[3], P-S.Iversen[4], J.N.Jackson[21], R.Jacobsson[44], P.Jalocha[16], G.Jarlskog[23], P.Jarry[39], B.Jean-Marie[18], E.K.Johansson[44], M.Jonker[7], L.Jonsson[23], P.Juillot[8], M.Kaiser[15], G.Kalmus[37], F.Kapusta[22], M.Karlsson[44], E.Karvelas[9], S.Katsanevas[3], E.C.Katsoufis[31], R.Keranen[7], B.A.Khomenko[14], N.N.Khovanski[14], B.King[21], N.J.Kjaer[28], H.Klein[7], A.Klovning[4], P.Kluit[30], A.Koch-Mehrin[52], J.H.Koehne[15], B.Koene[30], P.Kokkinias[9], M.Koratzinos[32], K.Korcyl[16], A.V.Korytov[14], V.Kostioukhine[42], C.Kourkoumelis[3], O.Kouznetsov[14], P.H.Kramer[52], M.Krammer[50], C.Kreuter[15], J.Krolikowski[51], I.Kronkvist[23], W.Krupinski[16], K.Kulka[48], K.Kurvinen[13], C.Lacasta[49], I.Laktineh[24], C.Lambropoulos[9], J.W.Lamsa[1], L.Lanceri[46], P.Langefeld[52], V.Lapin[42], I.Last[21], J-P.Laugier[39], R.Lauhakangas[13], G.Leder[50], F.Ledroit[12], R.Leitner[29], Y.Lemoigne[39], J.Lemonne[2], G.Lenzen[52], V.Lepeltier[18], T.Lesiak[35], J.M.Levy[8], E.Lieb[52], D.Liko[50], R.Lindner[52], A.Lipniacka[18], I.Lippi[35], B.Loerstad[23], M.Lokajicek[10], J.G.Loken[34], A.Lopez-Fernandez[7], M.A.Lopez Aguera[41], M.Los[30], D.Loukas[9], J.J.Lozano[49], P.Lutz[39], L.Lyons[34], G.Maehlum[15], J.Maillard[6], A.Maio[20], A.Maltezos[9], F.Mandl[50], J.Marco[41], B.Marechal[47], M.Margoni[35], J-C.Marin[7], C.Mariotti[40], A.Markou[9], T.Maron[52], S.Marti[49], C.Martinez-Rivero[41], F.Martinez-Vidal[49], F.Matorras[41], C.Matteuzzi[27], G.Matthiae[38], M.Mazzucato[35], M.Mc Cubbin[21], R.Mc Kay[1], R.Mc Nulty[21], J.Medbo[48], C.Meroni[27], W.T.Meyer[1], M.Michelotto[35], E.Migliore[45], I.Mikulec[50], L.Mirabito[24], W.A.Mitaroff[50], G.V.Mitselmakher[14], U.Mjoernmark[23], T.Moa[44], R.Moeller[28], K.Moenig[7], M.R.Monge[11], P.Morettini[11], H.Mueller[15], W.J.Murray[37], B.Muryn[16], G.Myatt[34], F.Naraghi[12], F.L.Navarria[5], P.Negri[27], S.Nemecek[10], W.Neumann[52], R.Nicolaidou[3], B.S.Nielsen[28], P.Niss[44], A.Nomerotski[35], A.Normand[34], V.Obraztsov[42], A.G.Olshevski[14], R.Orava[13], K.Osterberg[13], A.Ouraou[39], P.Paganini[18], M.Paganoni[27], R.Pain[22], H.Palka[16], Th.D.Papadopoulou[31], L.Pape[7], F.Parodi[11], A.Passeri[40], M.Pegoraro[35], J.Pennanen[13], L.Peralta[20], H.Pernegger[50], M.Pernicka[50], A.Perrotta[5], C.Petridou[46], A.Petrolini[11], H.T.Phillips[37], G.Piana[11], F.Pierre[39], M.Pimenta[20], S.Plaszczynski[18], O.Podobrin[15], M.E.Pol[17], G.Polok[16], P.Poropat[46], V.Pozdniakov[14], M.Prest[46], P.Privitera[38], A.Pullia[27], D.Radojicic[34], S.Ragazzi[27], H.Rahmani[31], J.Rames[10], P.N.Ratoff[19], A.L.Read[32], M.Reale[52], P.Rebecchi[18], N.G.Redaelli[27], M.Regler[50], D.Reid[7], P.B.Renton[34], L.K.Resvanis[3], F.Richard[18], J.Richardson[21], J.Ridky[10], G.Rinaudo[45], I.Ripp[39], A.Romero[45], I.Roncagliolo[11], P.Ronchese[35], L.Roos[12], E.I.Rosenberg[1], E.Rosso[7], P.Roudeau[18], T.Rovelli[5], W.Ruckstuhl[30], V.Ruhlmann-Kleider[39], A.Ruiz[41], K.Rybicki[16], H.Saarikko[13], Y.Sacquin[39], G.Sajot[12], J.Salt[49], J.Sanchez[25], M.Sannino[11], S.Schael[7], H.Schneider[15], M.A.E.Schyns[52],

G.Sciolla[45], F.Scuri[46], A.M.Segar[34], A.Seitz[15], R.Sekulin[37], R.Seufert[15], R.C.Shellard[36], I.Siccama[30], P.Siegrist[39], S.Simonetti[39], F.Simonetto[35], A.N.Sisakian[14], T.B.Skaali[32], G.Smadja[24], N.Smirnov[42], O.Smirnova[14], G.R.Smith[37], R.Sosnowski[51], D.Souza-Santos[36], T.Spassov[20], E.Spiriti[40], S.Squarcia[11], H.Staeck[52], C.Stanescu[40], S.Stapnes[32], I.Stavitski[35], G.Stavropoulos[9], K.Stepaniak[51], F.Stichelbaut[7], A.Stocchi[18], J.Strauss[50], J.Straver[7], R.Strub[8], B.Stugu[4], M.Szczekowski[51], M.Szeptycka[51], T.Tabarelli[27], O.Tchikilev[42], G.E.Theodosiou[9], Z.Thome[47], A.Tilquin[26], J.Timmermans[30], V.G.Timofeev[14], L.G.Tkatchev[14], T.Todorov[8], D.Z.Toet[30], A.Tomaradze[2], B.Tome[20], E.Torassa[45], L.Tortora[40], G.Transtromer[23], D.Treille[7], W.Trischuk[7], G.Tristram[6], C.Troncon[27], A.Tsirou[7], E.N.Tsyganov[14], M.Turala[16], M-L.Turluer[39], T.Tuuva[13], I.A.Tyapkin[22], M.Tyndel[37], S.Tzamarias[21], B.Ueberschaer[52], S.Ueberschaer[52], O.Ullaland[7], V.Uvarov[42], G.Valenti[5], E.Vallazza[7], J.A.Valls Ferrer[49], C.Vander Velde[2], G.W.Van Apeldoorn[30], P.Van Dam[30], M.Van Der Heijden[30], W.K.Van Doninck[2], J.Van Eldik[30], P.Vaz[7], G.Vegni[27], L.Ventura[35], W.Venus[37], F.Verbeure[2], M.Verlato[35], L.S.Vertogradov[14], D.Vilanova[39], P.Vincent[24], L.Vitale[46], E.Vlasov[42], A.S.Vodopyanov[14], M.Vollmer[52], M.Voutilainen[13], H.Wahlen[52], C.Walck[44], A.Wehr[52], M.Weierstall[52], P.Weilhammer[7], A.M.Wetherell[7], J.H.Wickens[2], M.Wielers[15], G.R.Wilkinson[34], W.S.C.Williams[34], M.Winter[8], M.Witek[7], G.Wormser[18], K.Woschnagg[48], K.Yip[34], O.Yushchenko[42], F.Zach[24], A.Zaitsev[42], A.Zalewska[16], P.Zalewski[51], D.Zavrtanik[43], E.Zevgolatakos[9], N.I.Zimin[14], M.Zito[39], D.Zontar[43], R.Zuberi[34], G.Zumerle[35]

[1] Ames Laboratory and Department of Physics, Iowa State University, Ames IA 50011, USA
[2] Physics Department, Univ. Instelling Antwerpen, Universiteitsplein 1, B-2610 Wilrijk, Belgium
and IIHE, ULB-VUB, Pleinlaan 2, B-1050 Brussels, Belgium
and Faculté des Sciences, Univ. de l'Etat Mons, Av. Maistriau 19, B-7000 Mons, Belgium
[3] Physics Laboratory, University of Athens, Solonos Str. 104, GR-10680 Athens, Greece
[4] Department of Physics, University of Bergen, Allégaten 55, N-5007 Bergen, Norway
[5] Dipartimento di Fisica, Università di Bologna and INFN, Via Irnerio 46, I-40126 Bologna, Italy
[6] Collège de France, Lab. de Physique Corpusculaire, IN2P3-CNRS, F-75231 Paris Cedex 05, France
[7] CERN, CH-1211 Geneva 23, Switzerland
[8] Centre de Recherche Nucléaire, IN2P3 - CNRS/ULP - BP20, F-67037 Strasbourg Cedex, France
[9] Institute of Nuclear Physics, N.C.S.R. Demokritos, P.O. Box 60228, GR-15310 Athens, Greece
[10] FZU, Inst. of Physics of the C.A.S. High Energy Physics Division, Na Slovance 2, 180 40, Praha 8, Czech Republic
[11] Dipartimento di Fisica, Università di Genova and INFN, Via Dodecaneso 33, I-16146 Genova, Italy
[12] Institut des Sciences Nucléaires, IN2P3-CNRS, Université de Grenoble 1, F-38026 Grenoble Cedex, France
[13] Research Institute for High Energy Physics, SEFT, P.O. Box 9, FIN-00014 Helsinki, Finland
[14] Joint Institute for Nuclear Research, Dubna, Head Post Office, P.O. Box 79, 101 000 Moscow, Russian Federation
[15] Institut für Experimentelle Kernphysik, Universität Karlsruhe, Postfach 6980, D-76128 Karlsruhe, Germany
[16] High Energy Physics Laboratory, Institute of Nuclear Physics, Ul. Kawiory 26a, PL-30055 Krakow 30, Poland
[17] Centro Brasileiro de Pesquisas Físicas, rua Xavier Sigaud 150, BR-22290 Rio de Janeiro, Brazil
[18] Université de Paris-Sud, Lab. de l'Accélérateur Linéaire, IN2P3-CNRS, Bat 200, F-91405 Orsay Cedex, France
[19] School of Physics and Materials, University of Lancaster, Lancaster LA1 4YB, UK
[20] LIP, IST, FCUL - Av. Elias Garcia, 14-1°, P-1000 Lisboa Codex, Portugal
[21] Department of Physics, University of Liverpool, P.O. Box 147, Liverpool L69 3BX, UK
[22] LPNHE, IN2P3-CNRS, Universités Paris VI et VII, Tour 33 (RdC), 4 place Jussieu, F-75252 Paris Cedex 05, France
[23] Department of Physics, University of Lund, Sölvegatan 14, S-22363 Lund, Sweden
[24] Université Claude Bernard de Lyon, IPNL, IN2P3-CNRS, F-69622 Villeurbanne Cedex, France
[25] Universidad Complutense, Avda. Complutense s/n, E-28040 Madrid, Spain
[26] Univ. d'Aix - Marseille II - CPP, IN2P3-CNRS, F-13288 Marseille Cedex 09, France
[27] Dipartimento di Fisica, Università di Milano and INFN, Via Celoria 16, I-20133 Milan, Italy
[28] Niels Bohr Institute, Blegdamsvej 17, DK-2100 Copenhagen 0, Denmark
[29] NC, Nuclear Centre of MFF, Charles University, Areal MFF, V Holesovickach 2, 180 00, Praha 8, Czech Republic
[30] NIKHEF-H, Postbus 41882, NL-1009 DB Amsterdam, The Netherlands
[31] National Technical University, Physics Department, Zografou Campus, GR-15773 Athens, Greece
[32] Physics Department, University of Oslo, Blindern, N-1000 Oslo 3, Norway
[33] Dpto. Fisica, Univ. Oviedo, C/P. Pérez Casas, S/N-33006 Oviedo, Spain
[34] Department of Physics, University of Oxford, Keble Road, Oxford OX1 3RH, UK
[35] Dipartimento di Fisica, Università di Padova and INFN, Via Marzolo 8, I-35131 Padua, Italy
[36] Depto. de Fisica, Pontificia Univ. Católica, C.P. 38071 RJ-22453 Rio de Janeiro, Brazil
[37] Rutherford Appleton Laboratory, Chilton, Didcot OX11 OQX, UK
[38] Dipartimento di Fisica, Università di Roma II and INFN, Tor Vergata, I-00173 Rome, Italy
[39] Centre d'Etude de Saclay, DSM/DAPNIA, F-91191 Gif-sur-Yvette Cedex, France
[40] Istituto Superiore di Sanità, Ist. Naz. di Fisica Nucl. (INFN), Viale Regina Elena 299, I-00161 Rome, Italy
[41] C.E.A.F.M., C.S.I.C. - Univ. Cantabria, Avda. los Castros, S/N-39006 Santander, Spain, (CICYT-AEN93-0832)
[42] Inst. for High Energy Physics, Serpukov P.O. Box 35, Protvino, (Moscow Region), Russian Federation
[43] J. Stefan Institute and Department of Physics, University of Ljubljana, Jamova 39, SI-61000 Ljubljana, Slovenia
[44] Fysikum, Stockholm University, Box 6730, S-113 85 Stockholm, Sweden
[45] Dipartimento di Fisica Sperimentale, Università di Torino and INFN, Via P. Giuria 1, I-10125 Turin, Italy
[46] Dipartimento di Fisica, Università di Trieste and INFN, Via A. Valerio 2, I-34127 Trieste, Italy
and Istituto di Fisica, Università di Udine, I-33100 Udine, Italy
[47] Univ. Federal do Rio de Janeiro, C.P. 68528 Cidade Univ., Ilha do Fundão BR-21945-970 Rio de Janeiro, Brazil
[48] Department of Radiation Sciences, University of Uppsala, P.O. Box 535, S-751 21 Uppsala, Sweden
[49] IFIC, Valencia-CSIC, and D.F.A.M.N., U. de Valencia, Avda. Dr. Moliner 50, E-46100 Burjassot (Valencia), Spain
[50] Institut für Hochenergiephysik, Österr. Akad. d. Wissensch., Nikolsdorfergasse 18, A-1050 Vienna, Austria
[51] Inst. Nuclear Studies and University of Warsaw, Ul. Hoza 69, PL-00681 Warsaw, Poland
[52] Fachbereich Physik, University of Wuppertal, Postfach 100 127, D-42097 Wuppertal 1, Germany

1 Introduction

After several years of successful LEP operation with rising statistics, there is excellent agreement between the data and Standard Model (SM) predictions in the energy region of the Z^0. However, previous experiments at LEP have not rigorously tested SM expectations away from the Z^0 pole. These predictions depend upon the precise understanding of the large effects of electromagnetic radiative corrections.

In this paper experimental results from studies of photons produced in $e^+e^- \to \mu^+\mu^-$ interactions at LEP energies are used to check our knowledge of electromagnetic radiative corrections and to probe cross sections and asymmetries in the unexplored energy region between LEP and TRISTAN, and indeed all the way down to PETRA energies.

Investigations in the unexplored energy region are encouraged by the reported $e^+e^- \to \mu^+\mu^-$ cross section measurement which is 2σ lower than the SM prediction at TRISTAN ($\sqrt{s} \sim 60$ GeV[†]) [1]. Measurable deviations in the $e^+e^- \to f\bar{f}$ cross section in this energy region are predicted by several models beyond the SM that introduce a hypothetical additional Z' boson.

This paper is organised as follows. Section 2 provides the theoretical background to this study. In Section 3 radiative $e^+e^- \to \mu^+\mu^-$ events, where the photons are detected in the electromagnetic calorimeters, are considered. Measurements of the angular and energy spectra of these predominantly final state photons are presented and a comparison with the theoretical predictions is made. Section 4 deals with events with mainly initial state photons, which are not detected in the electromagnetic calorimeters. These measurements test our understanding of initial state radiation and allow the underlying Born cross section and asymmetry to be measured at reduced effective centre-of-mass energies. Section 5 uses the cross section measurements below the Z^0 pole, together with the DELPHI measurements of hadronic cross sections and leptonic cross sections and asymmetries at LEP energies, to obtain limits on the parameters of additional Z' gauge bosons in several models. Finally, Section 6 provides a summary and conclusions.

2 Theoretical formalism

Electromagnetic radiative corrections to the interaction $e^+e^- \to f\bar{f}$ distort the Born-level cross section at energies around the Z^0 pole, so that the cross sections measured by the experiments at LEP ([2]–[5]) are substantially different from the Born-level formula.

Most of the effects (see [6] for a detailed review and compilation of references) can be understood to arise from initial state radiation, after which the effective annihilation energy of the e^+e^- is less than the overall centre-of-mass energy $\sqrt{s}$. Because the Born cross section varies rapidly across the Z^0 pole, the resulting changes in the cross section are large and need to be understood very precisely in order that the underlying electroweak physics can be studied.

The cross section for $e^+e^- \to \mu^+\mu^-$ has contributions from direct Z^0 and photon terms and $\gamma - Z^0$ interference. Radiative corrections can be conveniently divided into the following components :

(i) Emission of real photons from the incident and/or final state fermions.
(ii) Corrections to the Z^0 and γ propagators. These consist of loop diagrams involving any particles which couple to these bosons.

[†]Natural units are used throughout with $\hbar = c = 1$, both in specifying units and in formulae.

(iii) Vertex corrections. These involve virtual photons as well as any other particles which couple to the initial or final state fermions.
(iv) Box diagrams, involving the exchange of two bosons (γ,Z^0).

At the present level of precision, the box diagrams can be neglected. The effect of the vertex and propagator corrections can, to a very good approximation, be absorbed in a redefinition of the Born-level parameters, such that the structure of the Born-level formulae is retained. This is the Improved or Effective Born Approximation as described in [6],[7],[8].

Initial state purely QED corrections can be described by a radiator function $\mathcal{R}$[9], such that the observed cross section for $e^+e^- \to f\bar{f}$ can be written as:

$$\sigma^f_{obs}(s) \;=\; \int_{z_0}^{1} \sigma^f_W(sz)\cdot\mathcal{R}(z)dz \;, \tag{1}$$

where

$$\frac{4m_f^2}{s} \;=\; z_0 \;\leq\; z \;\leq\; 1$$

and the invariant mass of the produced fermion-pair is given by $s' = sz$.

The term σ^f_W is the Improved Born Approximation cross section for $e^+e^- \to f\bar{f}$, which can be expressed in terms of the lineshape parameters in an (almost) model independent way, as

$$\sigma^f_W(s) \;=\; \frac{\sigma_0^{\rm f}}{\left(1+\frac{3\alpha}{4\pi}\right)}\frac{s{\Gamma_{\rm Z}}^2}{\left(s-{\rm M_Z}^2\right)^2+\frac{{\rm s}^2{\Gamma_{\rm Z}}^2}{{\rm M_Z}^2}} \;, \tag{2}$$

where

$$\sigma_0^{\rm f} = \frac{12\pi\Gamma_e\Gamma_f}{{\rm M_Z}^2{\Gamma_{\rm Z}}^2} \tag{3}$$

is the pole cross section, defined in terms of the Z^0 mass M_Z, total width Γ_Z and the partial widths Γ_e and Γ_f for $Z^0 \to e^+e^-$ and $Z^0 \to f\bar{f}$ (f $\neq$ e) respectively. The term $(1+3\alpha/4\pi)$ is a QED correction. It can be seen from equation (1) that the observed cross section involves a convolution of $\sigma^f_W(sz)$ with the radiator function. A similar formula can be written for the case when selection criteria are applied to the final state muons or the photons produced. In addition, there is a small initial-final state radiation interference contribution to the cross section [6].

Whereas calculations based on an analytic approach can be made for the total cross section (or for certain cuts on the final state fermions), the spectra of the produced photons can only be predicted, at present, by Monte Carlo methods. In this paper the generator DYMU3 [10] has been used. It can produce up to two photons from initial state radiation plus one from the final state. Full second order corrections are used for the initial state, and first order exponentiation in the final state. The total cross section predictions of DYMU3 and ZFITTER [8] are within 1% of each other.

2.1 Preliminaries to obtaining Z′ limits

Despite the excellent performance of the SM so far, there is general agreement that it is not the 'final' theory. Attempts at unification theories generally predict additional

neutral heavy gauge bosons Z′, of mass $M_{Z'}$ larger than M_Z. Many possible models have been discussed in the literature [11,12] which modify the SM gauge group in different ways, leading to predictions of new particles. The models include compositeness and super-string inspired E_6 models, the left-right (L-R) symmetric models and the Y and Y_L models.

A direct search for Z′ boson decays to lepton pairs in $\overline{p}p$ collisions has been made by the CDF collaboration [13]; for the models considered the 95% confidence level limit is $M_{Z'} > 320$ GeV. Limits on Z′ parameters have also been obtained by combining previous LEP data and weak neutral-current, atomic-parity violation and M_W measurements [14]; for most models the 90% C.L. limits on the mixing angle $\theta_{Z'}$ (defined by equation 4) are $-0.01 < \theta_{Z'} < 0.01$ radians. These combined analyses in general take an indirect approach, where the data are used to obtain model independent quantities which are then compared to the predictions of Z′ models. This analysis follows a more direct approach, as previously used by L3 [15], where radiatively corrected cross sections and asymmetries are predicted for the Z′ models allowing direct fits to be made to these observed quantities, so that limits can be placed on the parameters of the models. Fits of the data to the predictions of these models are discussed in section 5.

The existence of a Z′ would mean that the observed mass eigenstate at ~ 91 GeV needs to be considered as a mixture of the unmixed Z^0 and $Z^{0'}$, predicting a shift in M_Z from its SM value [15,16], with the mixing described by a matrix using the mixing angle $\theta_{Z'}$:

$$\begin{pmatrix} Z \\ Z' \end{pmatrix} = \begin{pmatrix} \cos\theta_{Z'} & \sin\theta_{Z'} \\ -\sin\theta_{Z'} & \cos\theta_{Z'} \end{pmatrix} \begin{pmatrix} Z^0 \\ Z^{0'} \end{pmatrix}. \tag{4}$$

The angle $\theta_{Z'}$ is related to the mixed masses M_Z and $M_{Z'}$, and the light unmixed mass M_0 as follows:

$$\tan^2\theta_{Z'} = \frac{{M_0}^2 - {M_Z}^2}{{M_{Z'}}^2 - {M_0}^2}. \tag{5}$$

The mass M_0 is related to the weak mixing angle and M_W in the SM expression:

$$M_0 = \frac{M_W}{\sqrt{\rho}\cos\theta_W}. \tag{6}$$

where ρ is the usual electroweak parameter. The parametrisation used in the Y and Y_L models differs from that of the E_6 and L-R models, the mixing being described by λ^2_{Y,Y_L} [17].

Figure 1 shows the deviations in the Born level hadronic and muon-pair cross sections predicted by several Z′ models. The Z′ masses used are close to the 95% C.L. lower limit values, derived in section 5, with mixing parameter $\theta_{Z'}$ or λ^2_{Y,Y_L} in the middle of the 95% C.L. allowed range for the mass used.

In the energy range near to the Z^0 pole position, the additional bosons' direct contributions to the cross sections are small. The deviations from SM expectations arise primarily from interference effects of the hypothesized bosons and the existing ones (γ and Z^0). The pole region behaviour is influenced by the Z′-Z^0 interference amplitude, which changes sign at the pole, resulting in an enhancement of the cross section compared to the SM value around $\sqrt{s} = M_Z - \Gamma_Z/2$ and some reduction at energies larger than the pole energy. In the region currently accessible by direct or indirect means, the largest deviations occur in the $E_6(\chi)$ and Y models, with predicted muon-pair cross section values 8% lower than the SM predictions in the region $\sqrt{s} \sim 70$ GeV arising due to $\gamma - Z'$ interference.

3 Muon-pair events with detected photons

3.1 Event selection

A detailed description of the DELPHI detector can be found in [18]. In this analysis, the first stage in the procedure is the selection of the $e^+e^- \to \mu^+\mu^-$ final state, without any requirements or selection on the produced photons. This selection procedure is similar to that described in [3]. The analysed sample comes from all data taken by DELPHI up to and including the 1992 LEP run, corresponding to an integrated luminosity of 40.5 pb^{-1} or $\sim 1.1 \cdot 10^6$ Z^0 decays into hadrons and charged leptons. Events were retained if they satisfied the following selection criteria:

1. number of charged particles N_{ch} satisfies $2 \leq N_{ch} \leq 5$.
2. the two highest momentum charged particles must have $p > 20$ GeV.
3. for the two highest momentum charged particles, the projection of the impact parameters in the plane transverse to the beam direction should be smaller than 1.5 cm, the longitudinal distances z_1 and z_2 between the points of closest approach and the beamspot should be smaller than 4.5 cm, and $\mid z_1 - z_2 \mid < 4.0$ cm. For particles where the microvertex detector participated in the track fit the impact parameter cut is reduced to 0.4 cm.
4. the two highest momentum charged particles are required to be in the polar angle range $20^\circ < \theta < 160^\circ$.
5. the two highest momentum charged particles are required to be identified as muons using either the muon chambers, the hadron calorimeter, or the electromagnetic calorimeters, as described in [3].

3.2 Photon detection

Photons are detected using the HPC (High-density Projection Chamber, see [18]) and FEMC (Forward ElectroMagnetic Calorimeter). The angular acceptances of these calorimeters are $43^\circ < \theta < 137^\circ$ for the HPC and $10^\circ < \theta < 36.5^\circ$, $143.5^\circ < \theta < 170^\circ$ for the FEMC.

Due to the amount of material before the electromagnetic calorimeters, about 40% of the photons convert before they reach the calorimeters, causing inefficiency and affecting the reconstructed energy.

If the conversion occurs before the tracking detector (TPC), the positrons and electrons produced give rise to tracks in the TPC and result in further showers in the electromagnetic calorimeters. Such a conversion results in an original single photon being seen as a 'wide shower' of energy deposits in the calorimeters. The energy observed in the calorimeters is less than that of the original photon due to energy loss between the conversion point and the calorimeter.

A simple clustering of energy deposits in the electromagnetic calorimeters is performed in which the energies are added together and the momentum of the 'photon' is obtained by adding the momentum vectors of the component deposits as seen from the interaction region. The clustering is performed if the momentum vectors are within 10° of each other. The deposits are required to be further than 2° from the nearest muon, to prevent inclusion of energy due to the muons.

3.3 Correcting observed E_γ and $\alpha_{\mu\gamma}$ distributions

Distortions of the true physics distributions due to detector effects were considered to be split into energy smearing, efficiency and purity components. Simulated $\mu^+\mu^-$ events generated using DYMU3 [10] and the full DELPHI simulation package were used to determine these quantities as functions of photon energy E_γ and the angle $\alpha_{\mu\gamma}$ between the momentum vectors of the photon and the nearer muon. A technique of obtaining a photon detection efficiency entirely from the data was developed and was applied both to the data and to the simulation events; this was used as a cross-check of the efficiency from the detector simulation. The simulation detection efficiencies of the muons and of the photon in the same event were found to be uncorrelated.

3.4 Photon energy smearing, efficiency and purity

A correction representing the smearing effect of the calorimeters' energy reconstruction was obtained from the ratio of the generated and measured energy distributions for events with an observed isolated photon cluster, where the directions of the observed cluster and the generated photon are within 1°. The definition of an isolated photon cluster used here, and in subsequent discussion unless otherwise specified, was that $\alpha_{\mu\gamma} > 5°$ and $E_\gamma > 2$ GeV, the cuts being applied to the appropriate generated or reconstructed quantities. The effect of smearing was to shift the apparent energy by a factor of 1.10 for energies above 10 GeV, the correction dipping to 0.79 for the lowest energy bin of 2–4 GeV. The photon detection efficiency from the simulation, ϵ_s, was defined as the fraction of events with a generated isolated photon, within the active acceptance of the calorimeters, in which an isolated photon cluster was reconstructed. The purity was defined as the fraction of events with observed isolated photon clusters that have one or more generated isolated photons. In obtaining the efficiency and purity as functions of photon energy E_γ, the energy correction was initially applied to the observed photon energy distribution in order to obtain the efficiency and purity without the effects of energy smearing. No such correction was required for $\alpha_{\mu\gamma}$ as the observed and generated angles were found to be almost identical. For energies above 10 GeV, ϵ_s was found to be approximately constant at 87% with purity greater than 98%. In the energy bin 4–6 GeV the efficiency dropped to 78% with purity down to 93%. As a function of $\alpha_{\mu\gamma}$, ϵ_s was found to be constant at 77% within the range 15–100°.

3.5 Efficiency from the data by kinematic reconstruction

The photon detection efficiency from the data, ϵ_r, was determined using the kinematically predicted photon direction and energy obtained by assuming the final state topology $\mu^+\mu^-\gamma$ (the reconstruction technique is described in section 4.4.1). This data efficiency was defined as the fraction of events predicted to have an isolated photon ($\alpha_{\mu\gamma} > 5°$, E_γ(predicted)$>$ 10 GeV) within the active acceptance of the calorimeters that are found to have an isolated photon cluster close to the expected position. The criterion for a successful prediction was that the angle between the predicted and measured photon directions was less than 15°. For photons of energy above 10 GeV the fraction of events satisfying this criterion was 93%. To attain a detection efficiency that can sensibly be compared to the efficiency from simulation it was first necessary to correct this efficiency to account for the effectiveness of the reconstruction. This reconstruction correction factor, obtained from the data, was defined as the fraction of events with observed isolated

clusters ($\alpha_{\mu\gamma} > 5°$, E_γ(meas)> 10 GeV) for which there is a successful prediction of photon position. The reconstruction correction factors as a function of $\alpha_{\mu\gamma}$ were found to be approximately constant for $\alpha_{\mu\gamma} > 5°$ at 0.90 from the data and 0.98 from simulation. Similar behaviour was observed as a function of E_γ with constant values of 0.84 from data and 0.98 from simulation for $E_\gamma > 15$ GeV.

Applying these correction factors yields $\epsilon_r(data)$ and $\epsilon_r(sim)$ from data and simulation as a function of E_γ and $\alpha_{\mu\gamma}$. They all exhibited similar behaviour, rising from values as low as 50% in the lowest energy (2–4 GeV) and angle (5–10°) bins up to a plateau value for $E_\gamma > 12$ GeV and for $\alpha_{\mu\gamma} > 25°$. The plateau value for $\epsilon_r(\alpha_{\mu\gamma})$ was 84% for both data and simulation, whereas for $\epsilon_r(E_\gamma)$ the value was 80% from data and 83% from simulation. These compare with $\epsilon_s(\alpha_{\mu\gamma})$ of 77% and $\epsilon_s(E_\gamma)$ of 87%, as described in section 3.4.

In the E_γ case a ratio of $\epsilon_r(data)$ and $\epsilon_r(sim)$ was used as a correction factor to apply to the efficiency from simulation ϵ_s; this yields a photon detection efficiency of 84%. An overall systematic error of 8% was assigned to the efficiency, based on the results of the above studies. The statistical errors on these efficiencies are significantly smaller than the estimated systematic error.

The data used encompass two significantly different high voltage settings for the HPC. No significant effect on the detection efficiency of isolated photons was observed due to this change.

3.6 Results on radiative $\mu^+\mu^-$ events

The total number of $\mu^+\mu^-$ events satisfying the selection criteria is 46561($N_{\mu+\mu-(\gamma)}$), of which 1682 have isolated photons seen in the calorimeters. The energy and angular spectra of these isolated photons are given in Figure 2 where the corrected data distributions are compared to the true distributions from simulation; the normalisation is to the number of $\mu^+\mu^-$ events. The ratio of the number of events with isolated photons to the total for data and simulation is given in Table 1.

There are no significant deviations between the energy and angular spectra obtained and the predictions of the DYMU3 simulation, at the present level of statistics and understanding of the systematics. The small deviation in the energy range 18–30 GeV is not considered to be significant. The results are in agreement with an analysis of radiative lepton events by the OPAL collaboration [19]; the results here are based on 6 times higher statistics.

$N_{\mu+\mu-(\gamma)}$	46561
$N_{\mu+\mu-(n\gamma);n\geq1}$ isolated photons	1682
$N_{\mu+\mu-(n\gamma);n\geq1}$ / $N_{\mu+\mu-(\gamma)}$ (Data)	$3.61 \pm 0.09\%$
$N_{\mu+\mu-(n\gamma);n\geq1}$ / $N_{\mu+\mu-(\gamma)}$ (Monte Carlo)	$3.74 \pm 0.06\%$

Table 1: The numbers of muon-pairs and of events with 'isolated photons' (as defined in section 3.2). The ratio of these numbers is compared with the DYMU3 simulation prediction after the full detector simulation (statistical errors only).

4 The reaction $e^+e^- \to \mu^+\mu^-$ with $M_{\mu\mu} < M_Z$

The bulk of the radiative effects on the cross section σ and asymmetry A_{FB} are due to initial state radiation; events with initial state photons can be considered to have an effective interaction energy below that of the Z^0 peak. The identification of muon-pair events with predominantly initial state radiation[‡] allows these effects to be isolated, enabling the underlying Born cross section and asymmetry to be measured at reduced effective centre-of-mass energies $\sqrt{s'}$ or $M_{\mu\mu}$; this provides the only way at present to probe the energy region between TRISTAN and LEP.

It is possible to make a distinction between events with predominantly initial state photons or predominantly final state photons due to the very different angular distributions of the produced photons in these processes, as shown in Figure 3. Initial state photons are mainly produced at small angles to the beam direction whereas final state photons are produced close to the direction of the muons, as shown in Section 3. Initial state photons will, in most cases, not be seen in the calorimeters of the detector, but go down the beam-pipe.

Events with predominantly initial/final state radiation are termed ISR/FSR events. The definition of a generated ISR event is that the total energy of initial state photons is greater than 1 GeV and the total energy of any final state photons is less than 1 GeV. A generated event is classified as FSR if the total energy of final state photons is greater than 1 GeV.

The dominance of FSR events over ISR events, in the low mass region, is illustrated in Table 2, where the distribution of ISR and FSR events in intervals of the $\mu^+\mu^-$ invariant mass,$M_{\mu\mu}$, is shown. This FSR dominance adds to the difficulty of making a relatively pure selection of ISR events. High statistics are necessary for this study, due to the steeply falling energy spectra of initial state radiation ($\sim 1/E_\gamma$) and also due to the very small relative cross section in this energy region.

$M_{\mu\mu}$ [GeV]	31-38	38-45	45-52	52-59	59-66	66-73	73-80
N_{FSR}	325	994	1216	1828	4469	7052	11862
N_{ISR}	144	129	115	127	138	197	398

Table 2: Numbers of ISR/FSR events obtained from $\sim 0.7 \cdot 10^6$ DYMU3 generated muon-pairs, in bins of $M_{\mu\mu}$.

4.1 ISR event selection procedure overview

Two approaches are taken to implement this selection:

A Cuts are applied to quantities affected by the presence of the photon, such as the acollinearity and acoplanarity of the event; and events with significant energy detected in the calorimeters are rejected.

B The photon parameters are reconstructed from the measured muon parameters by means of a kinematic fit (using the constraints from energy-momentum conservation) assuming only one photon is produced; then cuts are applied to the photon parameters.

[‡]The distinction between initial and final state photons is, of course, not strictly valid in a quantum mechanical interpretation. However, this distinction is made in the DYMU3 generator and allows a simplified discussion.

Approach **A** limits the kinematically allowed directions and energies of produced photons and thus its consequences are similar to approach **B**. The advantage of technique **B** is that it makes use of all available information allowing the effective centre-of-mass energy to be obtained with greater accuracy, as well as being the most direct technique once the photon parameters have been obtained. Technique **A** has the advantage of simplicity and for high energy photons (of energy greater than 10 GeV) equivalent results are expected. Both approaches have been pursued, allowing cross-checks to be made.

4.2 Selection of $e^+e^- \to \mu^+\mu^-(\gamma)$ events

Before the above selections can be made it is necessary to select muon-pair events, without biasing against radiative events. Clearly this requires a loose event selection, without the collinearity and high muon momenta cuts that are usually made in muon-pair analyses. This will result in higher backgrounds from $e^+e^- \to \tau^+\tau^-$ and 2-photon reactions: $e^+e^- \to e^+e^-\mu^+\mu^-$, $e^+e^- \to e^+e^-\tau^+\tau^-$. However, as investigated in section 4.6, the subsequent cuts to select $e^+e^- \to \mu^+\mu^-(\gamma)$ events (with predominantly initial state photons) result in very small tau-pair and 2-photon physics backgrounds.

The same selection as in section 3.1 is used apart from the momentum cut which is loosened to the requirement that the highest momentum charged particle must have $p > 12$ GeV, and the second highest momentum charged particle must have $p > 7$ GeV.

4.3 Selection A: acollinearity and acoplanarity cuts

For $\mu^+\mu^-\gamma$ events, where the photon has energy ≥ 10 GeV and momentum vector at a small angle to the beam direction, one expects a large acollinearity θ_{acol} due to the large Lorentz boost of the muon centre-of-mass system. Due to the small momentum component of the photon in the transverse plane, a small acoplanarity θ_{acop} is expected.

As the principal criteria of this selection are based on the angular cuts, the first step is an estimation of the quality of acollinearity/acoplanarity reconstruction. Studies of the differences between reconstructed and generated acollinearity/acoplanarity show that typical errors are 0.05^{O}. This good angular resolution allows the angular cuts to be studied using the DYMU3 generated events not passed through the full detector simulation, thus allowing high statistics studies to be made.

4.3.1 Generator level study of angular cuts

A total of $3.8 \cdot 10^5$ generated events was used (corresponding to approximately ten times higher statistics than the real $\mu^+\mu^-$ events). As indicators of the effectiveness of the selection, an efficiency and contamination are defined by:

$$S_i = \frac{N_i^{cut}}{N_i}, \qquad S_f = \frac{N_f^{cut}}{N_f^{cut} + N_i^{cut}},$$

where N_i (N_f) is the total number of $\mu^+\mu^-$ selected events where the highest energy photon is initial(final) state and N_i^{cut} (N_f^{cut}) are the numbers of $\mu^+\mu^-$ selected events after applying the acollinearity/acoplanarity cuts. S_i is the efficiency for selection of events with predominantly initial state photons and S_f shows the contamination of final state photon events in the sample.

Studies of the behaviour of S_i and S_f in various $\mathrm{M}_{\mu\mu}$ intervals for different angular cuts have been made; figure 4 shows the behaviour for the mass interval $73 < \mathrm{M}_{\mu\mu} < 80$ GeV.

The curves show S_i and $1 - S_f$ (the purity) as a function of θ^{cut}_{acop}, where $\theta_{acop} < \theta^{cut}_{acop}$, for $\theta_{acol} > 2,\ 5,\ 8,\ 11,\ 14$ degrees, with an additional cut requiring the absence of photons with energy greater than 3 GeV in the acceptance of the electromagnetic calorimeters. The values of S_i and $1 - S_f$ shown here are higher than can be achieved in practice, due to the effects of momentum smearing and photon detection inefficiency. The general behaviour of S_i and S_f is found to be the same in all the mass intervals.

The angular cuts in the mass intervals are chosen so as to optimise S_i, S_f and keep the τ background negligibly small; large θ^{cut}_{acol} and θ^{cut}_{acop} result in S_i, S_f close to their asymptotic values. The cuts chosen in the various mass intervals are presented in Table 3.

$M_{\mu\mu}$ in GeV	17 - 38	38 - 45	45 - 52	52 - 59	59 - 66	66 - 73	73 - 80
$\theta_{acol} >$	15	15	15	15	15	12	7
$\theta_{acop} <$	15	10	9	9	6	4	4

Table 3: Acollinearity and acoplanarity cut values used (degrees)

A sample of $5.6 \cdot 10^4$ fully simulated muon-pair events with high energy photons was produced by performing the simulation for events with muon-pair invariant mass, at the generator level, of less than 84 GeV. Within this limited mass range the sample allows distributions equivalent to those obtainable from $8.9 \cdot 10^5$ fully simulated muon-pair events.

The angular and energy distributions of the radiated photon, after angular cuts have been applied, are presented in Figure 5 for initial and final state photon events. It can be seen that the FSR classed events have θ_γ in the approximate range 20–160°. This arises due to the 20° cut on the polar angle of the muons together with the small angles between the muon and final state photon directions. The structure in E_γ arises from the restricted mass interval of Figure 5 imposing an allowed range in photon energy of 10–16 GeV; the few events with E_γ outside this band arise due to the presence of more than one significant photon in the event.

The FSR event dominance after the angular cuts demonstrates the necessity of a veto against events in which a hard photon is seen in the calorimeters for this selection. Details of photon detection techniques and efficiencies have been discussed in section 3.2.

The cuts are chosen to keep FSR contamination $\sim 15\%$ for large $M_{\mu\mu}$; it is practically zero for small $M_{\mu\mu}$.

4.3.2 Selection A criteria

The selection requires:

(1) The invariant mass of the muon-pair $M_{\mu\mu} < 80$ GeV.
(2) The acollinearity angle $> \theta^{cut}_{acol}$ depending on the mass interval, as shown in Table 3.
(3) The acoplanarity angle $< \theta^{cut}_{acop}$ depending on the mass interval.
(4) No clusters in HPC and FEMC with energy greater than 3 GeV.

A "true initial state event" is defined as having $\Sigma E_{\gamma(initial)} \geq 1$ GeV and $\Sigma E_{\gamma(final)} \leq 1$ GeV. After all the cuts the fraction of "true" ISR events that are selected is at the level of 70%. The FSR contamination $\sim 15\%$ for $E_\gamma < 15$ GeV and is small for more energetic photons.

4.4 Selection B : reconstructed unseen photon method

The first step is to reconstruct the unseen photon parameters from the muon momentum vectors and then devise a selection scheme based on these parameters. The angle of the photon to the beam direction is the principal quantity of use for the selection of events dominated by initial state photons.

4.4.1 Technique for reconstruction of unseen photons

The assumption of three-body kinematics allows an unseen photon to be reconstructed by performing a one constraint kinematic fit using the parameters and full error matrices of the muons. The basic hypothesis is that only one photon is radiated in the event. Neglecting the small energy spread in the energies of the incident particles prior to radiating, there are 9 variables: 6 muon parameters $1/p_1$,θ_1,ϕ_1,$1/p_2$,θ_2,ϕ_2 and 3 for the photon E_γ,θ_γ,ϕ_γ. The kinematic fitting approach used is described in [20].

On completion of the fit the 3 photon parameters can be unambiguously calculated from the muon parameters, with energy-momentum conservation being satisfied after the fit. The χ^2 obtained on completion of the fit provides an indicator that the assumption of a single radiated photon was correct; the resultant 3-vector for the photon was then used in subsequent analysis.

Other fits are also performed using the same approach as described above, but making different assumptions about the topology. The hypotheses tried and corresponding χ^2 probabilities are:

(1) $\mu\mu\gamma$ (1 constraint fit), P(1γ).
(2) $\mu\mu$ with no photons produced (4 constraints), P(0γ).
(3) $\mu\mu\gamma$ where the single photon goes in the beam direction (3 constraints).

4.4.2 Performance of the reconstruction

The performance of the reconstruction of the photon angles can be seen from Figure 6. The comparitively small number of events with two photons, each of energy greater than 1 GeV, shown in the shaded portion of Figure 6, indicates that the primary cause of poor photon reconstruction is the finite muon momentum resolution rather than events with two hard photons. Due to this there is a photon energy below which it is impossible to distinguish an event as having a photon or not. In order to remove soft photon events without imposing too severe an acollinearity cut (or equivalently a photon energy cut) that would limit the range of $\sqrt{s'}$ under study, the χ^2 probability P(0γ) is used. This probability indicates how consistent an event is with the hypothesis that no hard photons were produced.

Figure 7 shows the consistency of the data events with the two hypotheses of either 1 photon produced or no photons. The small population in the region of high $P(0\gamma)$ and low $P(1\gamma)$ is because events with a low probability in the one photon fit cannot have a high probability in the more constrained zero photon fit.

The "wall" of events at low $P(0\gamma)$ contains the events of interest. Events with high energy photons in the mass range $M_{\mu\mu} < 86$ GeV are selected by requiring $P(0\gamma) \leq 10^{-2}$ and $P(1\gamma) \geq 10^{-2}$, thus ensuring accurate reconstruction of the unseen photon parameters. The ISR/FSR distinction is made by requiring that the reconstructed photon has an angle to the beam direction θ_γ of less than 20° and an angle to the nearer muon, $\alpha_{\mu\gamma}$, of greater than 10°; also it is demanded that no electromagnetic clusters with energy greater than 3 GeV are present in the HPC or FEMC.

4.4.3 Obtaining the effective centre-of-mass energy

The performance of the reconstruction and selection is shown in Figure 8, by comparison of the reconstructed and true photon energies. In 71% of the selected events the photon energy is reconstructed to within 1 GeV. However there is a tendency for events with a low energy photon or with no photon to have too high a reconstructed energy. The events with two hard photons, shaded in the figure, can be seen to constitute an overall impurity of $\sim 6\%$ within the selection.

As a cross-check of the energy reconstruction, the effective energy was calculated using the additional assumption that the photon direction is along the beam direction. This allows the photon energy to be calculated using energy-momentum conservation and assuming zero mass for the muons:

$$E_\gamma = \frac{|\sin(\theta_1+\theta_2)|}{|\sin(\theta_1+\theta_2)| + \sin\theta_1 + \sin\theta_2}\sqrt{s},$$

leading directly to the effective centre-of-mass energy or, equivalently, the muon-pair invariant mass $\sqrt{s'}$,

$$s' = s - 2E_\gamma\sqrt{s}.$$

Simulation studies indicate that this $\sqrt{s'}$ is somewhat closer to the true effective centre-of-mass energy than the $\sqrt{s'}$ obtained from the fit once the selection of ISR events has been made.

4.4.4 Selection B criteria

Using the χ^2 probabilities of the fits assuming $\mu^+\mu^-$, $P(0\gamma)$, and assuming $\mu\mu\gamma$, $P(1\gamma)$ and the reconstructed photon parameters, the selection is made as follows:

(1) Event should not be consistent with $\mu^+\mu^-$, having $P(0\gamma) \leq 10^{-2}$
(2) For the $\mu\mu\gamma$ fit, require $P(1\gamma) \geq 10^{-2}$
(3) Angle between photon and beam direction $\theta_\gamma \leq 20°$
(4) Angle between photon and nearer muon $\alpha_{\mu\gamma} \geq 10°$
(5) No clusters in HPC and FEMC with energy greater than 3 GeV

The additional cut (5) results in a gain in the purity of $\sim 4\%$ in the mass region above 85 GeV.

4.5 Comparison and cross-checks of the two selections.

High statistics generator studies have been used to test the effectiveness of the selections. To match the data, the DYMU3 generated muon parameters are smeared with θ dependent errors on $\delta(1/p)$, and angular errors $\delta\theta$, $\delta\phi = 1$ mrad. In performing the generator level studies the initial or final state character of the photons is known, allowing purities and efficiencies of the selections to be obtained; in addition high statistics can be used.

Using the definition of "true initial state events" in section 4.3.2, the efficiency and purity are defined as follows:

- Efficiency: the fraction of the "true initial state events" that are selected (assuming all such events occur within the $\mu^+\mu^-$ preselection).
- Purity: the fraction of the selected events that are "true initial state events".

Figure 9 shows the purity and efficiency as a function of the effective energy $\sqrt{s'}$ for selection **B**. Selection **B** has a higher efficiency than selection **A**. The purities are within 5% of each other, with selection **B** performing better at low $M_{\mu\mu}$, and also at high mass where technique **A** cannot be applied.

4.6 Backgrounds from $\tau^+\tau^-$ and two-photon interactions

Due to the requirement of selecting muon-pair events without biasing against radiative events, a very loose $\mu\mu(\gamma)$ preselection is applied, resulting in a relatively large $\tau\tau$ background within the preselection. However, on subsequently applying either of the initial state event selections **A** and **B**, this background is almost entirely removed. Simulation studies using ~ 93000 generated tau-pairs and $\sim 1.3 \cdot 10^5$ generated muon-pairs, passed through the full detector simulation, lead to tau backgrounds of 0.32% in selection **A** and 0.64% in selection **B**, corresponding to less than one tau-pair event in each of the samples.

Possible backgrounds from γ-γ interactions, have been investigated using ~ 68000 generated $e^+e^- \to e^+e^-\mu^+\mu^-$ events and ~ 10000 $e^+e^- \to e^+e^-\tau^+\tau^-$ events, passed through the full detector simulation. The predicted $e^+e^- \to e^+e^-\mu^+\mu^-$ backgrounds in selections **A**(**B**) were found to be $\sim 3(2)$ events respectively, whereas less than 1 $e^+e^- \to e^+e^-\tau^+\tau^-$ event was expected in the samples. The γ-γ backgrounds were found to occur predominantly at low effective energies $\sqrt{s'} < 40$ GeV. No correction was applied to account for these small backgrounds.

4.7 Obtaining $\sigma(e^+e^- \to \mu^+\mu^-)$ and $A_{FB}(e^+e^- \to \mu^+\mu^-)$

As the number of ISR events is, to a good approximation, proportional to the cross section an indirect measurement of the Born cross section at $\sqrt{s'}$ is obtained by scaling the SM expectation of the mean Born cross section in the energy range by the ratio of the number of events observed to the number expected from simulation. The normalization was performed by comparing the number of $e^+e^- \to \mu^+\mu^-$ events as selected in section 3.1 in data and simulation.

This technique clearly relies on the correct simulation of detector performance in measuring the muon parameters. The expected final state radiation background in the $M_{\mu\mu}$ bins (obtained from a simulation study) cannot be corrected for in the determination of the cross section without independent knowledge of the impurity in the data sample. It is because of the difficulty of correcting for this background that it is important that a high purity selection is used.

In calculating the forward-backward asymmetry (defined in [3]) for events which are far from being back-to-back, it is more satisfactory to deal with the angle made by the μ^+ or μ^- to the beam direction in the $\mu^+\mu^-$ rest frame, θ^* [21]. This is given by:

$$\cos\theta^* = \frac{\sin\frac{1}{2}(\theta_2 - \theta_1)}{\sin\frac{1}{2}(\theta_2 + \theta_1)}$$

where θ_1 and θ_2 are the measured polar angles of μ^+ and μ^- in the laboratory frame. Thus the asymmetry can be obtained directly from the data, without recourse to comparisons between data and simulation.

High statistics generator level studies, as mentioned in the previous section with regard to testing the selection, are also used to test the method. Figure 10 and Table 4 show the muon-pair asymmetry obtained from data, from fully simulated Monte Carlo events and

from $5.3 \cdot 10^6$ generated muon-pair events, momentum smeared and then reconstructed, using selection **B**. The dashed curve is the Born asymmetry and the solid curve is 80% of the Born asymmetry.

As the impurity events (final state photon or no hard photon events) have an effective energy on the peak (where the asymmetry is close to zero), their effect on the asymmetry is to make it less negative. For an impurity of $\sim$ 20% one would expect an asymmetry of $\sim$ 80% of the Born asymmetry; this expected behaviour is exhibited in Figure 10 with the points closely following the solid 80% Born asymmetry curve.

4.8 Results

Up to and including the LEP run of 1992, corresponding to 46561 selected muon-pairs, a total of 76(90) events with interaction energy between 17 GeV and 80 GeV are collected in selections **A**(**B**); 51 of these events are common to the two selections. The number of events observed in $M_{\mu\mu}$ bins for the data and simulation using selection **A**, and the calculated cross sections are presented in Table 5.

The mass region above 80 GeV is also probed by selection **B**. The results are presented in Table 5, and Figure 11. Studies of the effect on the results of using three different techniques to reconstruct the effective energy were made. The techniques used were the $M_{\mu\mu}$ calculated from the measured muon parameters, the effective energy obtained from the fit assuming a $\mu\mu\gamma$ topology, and also the energy calculated assuming a single initial state photon to be travelling in the beam direction. The resulting variations in the cross section were less than 20%.

All the measured cross sections (Figure 11 and Table 5) and the measured asymmetries (Figure 10 (a) and Table 4) are compatible with the expectations of the Standard Model.

5 Obtaining Z′ limits

Several extensions to the Standard Model incorporating a hypothetical additional Z′ boson of mass $M_{Z'}$, with $M_{Z'} > M_Z$, were introduced in section 2.1. In this section we compare predictions of the effects of Z′ in several models to the observations, as a function of the parameters of the models. In this way we put limits on these parameters. The extended gauge models considered are :

E_6 model [22] This is a superstring-inspired model. Different mixing regimes of Z′ to fermions were considered, with $\Theta_6 = 0$, $\pi/2$ and $-\arctan\sqrt{5/3}$ defining the $E_6(\chi)$, $E_6(\psi)$ and $E_6(\eta)$ models respectively.

L-R model [23] Left-right symmetric models include a right-handed $SU(2)_R$ extension to the Standard Model gauge group $SU(2)_L \otimes U(1)$. The parameter $\alpha_{\mathrm{L-R}}$ describes the couplings of the heavy bosons to fermions, and it can be expressed in terms of the $SU(2)_{L,R}$ coupling constants $g_{L,R}$ and the weak mixing angle. For $\alpha_{\mathrm{L-R}}$ at its lower bound of $\sqrt{2/3}$, the L-R model is identical to the $E_6(\chi)$ model. The upper bound corresponds to $g_L = g_R$ with value $\alpha_{\mathrm{L-R}} \sim 1.53$ for $\sin^2\theta_w = 0.23$. Different mixing regimes were considered, corresponding to $\alpha_{\mathrm{L-R}} = 1$ and $\alpha_{\mathrm{L-R}} = \sqrt{2}$.

Y model [12,17] Compositeness-inspired model extending the SM gauge group with $U(1)_{B-L}$.

$M_{\mu\mu}$ [GeV]	10-30	30-50	50-64	64-74	74-84	84-91
$A_{fb}(da)$	0.09	0.07	-0.11	-0.62	-0.56	-0.13
$\delta A_{fb}(da)$	0.30	0.26	0.33	0.17	0.10	0.05
$A_{fb}(mc)$	-0.08	-0.11	-0.26	-0.41	-0.63	-0.17
$\delta A_{fb}(mc)$	0.12	0.06	0.07	0.05	0.03	0.02

$M_{\mu\mu}$ [GeV]	10-24	24-38	38-52	52-66	66-73	73-80	80-84	84-88	88-91
$A_{fb}(ge)$	-0.01	-0.04	-0.15	-0.30	-0.49	-0.55	-0.57	-0.40	-0.15
$\delta A_{fb}(ge)$	0.02	0.03	0.03	0.02	0.02	0.02	0.02	0.01	0.01

Table 4: Asymmetry in bins of effective energy for data, full simulation and smeared DYMU3 generated events, using selection **B**.

Selection **A**

$M_{\mu\mu}$ [GeV]	17-24	24-31	31-38	38-45	45-52	52-59	59-66	66-73	73-80
N(obs)	2	5	7	4	6	6	5	12	29
N(mc)	2.3	4.0	5.2	6.0	5.1	7.0	9.3	13.2	24.5
N(fsr)	0.0	0.1	0.2	0.4	0.4	0.8	1.5	1.0	3.9
σ [pb]	206.	165.	113.	39.	51.	28.	15.0	22.4	34.0
δ_σ [pb]	145.	74.	43.	19.	21.	12.	6.7	6.5	6.3
$\sigma_{\rm Born}$ [pb]	238.4	130.8	82.8	57.3	42.3	33.0	27.4	25.1	29.1

Selection **B**

$M_{\mu\mu}$ [GeV]	17-24	24-31	31-38	38-45	45-52	52-59	59-66	66-73	73-80	80-84	84-86
N(obs)	4	5	6	8	7	4	8	14	34	45	40
N(mc)	1.7	5.2	3.5	6.6	5.7	6.1	10.5	16.6	30.1	37.1	37.1
N(fsr)	0.0	0.4	0.0	0.0	0.0	0.4	0.9	0.4	2.6	2.6	3.9
σ [pb]	545.9	124.8	142.2	70.0	52.2	21.6	20.9	21.2	32.8	58.3	94.1
δ_σ [pb]	386.0	66.4	76.8	30.6	24.5	12.2	8.5	6.6	6.9	10.7	18.0
$\sigma_{\rm Born}$ [pb]	238.4	130.8	82.8	57.3	42.3	33.0	27.4	25.1	29.1	48.1	87.3

Table 5: Observed and expected numbers of events for different $M_{\mu\mu}$ intervals from data N(obs) and simulation N(mc), and the calculated cross sections with statistical errors, δ_σ, using selections **A** and **B**. The mean Born level cross section within the energy ranges, $\sigma_{\rm Born}$, and also the prediction from simulation of the final state radiation background in the data sample N(fsr) are provided.

Y_L model [12,17] Compositeness-inspired model where the gauge boson associated with an additional group is coupled to the left component of the hypercharge current only.

5.1 E_6 and L-R models

The effects of Z′ for the L-R and E_6 models on the cross sections and asymmetries were calculated using an addition to the ZFITTER (version 4.5)[8] program, called ZEFIT (version 3.1)[16] that provides radiatively corrected cross sections and asymmetries, optionally with cuts applied, for the processes $e^+e^- \to l^+l^-$ and $e^+e^- \to$ hadrons. The calculation used the input parameters: Z^0 mass M_Z, top quark mass M_t, Higgs mass M_H, and the strong coupling constant at the Z^0 pole α_S, together with additional parameters due to the Z′: $M_{Z'}$ and the mixing angle $\theta_{Z'}$.

The data used for the fits were the measurements from 1990 to 1992 of the hadronic cross section and leptonic cross sections and asymmetries for the three flavours, reported in [3]. In addition, the $e^+e^- \to \mu^+\mu^-$ cross section measurements in the energy range 17–86 GeV from the data collected up to and including 1992, as obtained in section 4.8 using selection **B**, were also used. Equivalent results were obtained from fits performed to data using selection **A**. It was found that the contribution of the low energy cross section measurements to the determination of the models' parameters was small for the E_6 and L-R models, the χ^2 contours only changing slightly with the addition of these data.

To reduce the number of parameters, α_S was fixed at the value determined by the DELPHI experiment [24] of $\alpha_S = 0.123$, and the fits were performed for a series of top quark and Higgs boson masses, $M_t = 100, 150, 200$ GeV and $M_H = 60, 300, 1000$ GeV. A χ^2 was formed comparing the measured and predicted values of the cross sections and asymmetries. A full covariance matrix treatment of the errors was performed for the on-peak data, with complete account being taken of the LEP energy uncertainties and their point-to-point correlations. As the standard Z^0 mass changes due to the presence of Z′, M_Z was left free in the fit, along with the mass and mixing angle of Z′.

The Z^0 mass resulting from the fits was found to deviate from the SM fit result (assuming no Z′) by less than 0.004 GeV. For each fit the 95% C.L. allowed region in the $M_{Z'}$,$\theta_{Z'}$ plane was obtained as the region where $\chi^2 < \chi^2_{min} + 5.99$. The results of the fits are presented in Table 6 for $M_t = 150$ GeV and $M_H = 300$ GeV. The 95% C.L. allowed ranges of $\theta_{Z'}$ are given, and also the lower limits of $M_{Z'}$ for both $\theta_{Z'} = 0$, as well as for any $\theta_{Z'}$. Comparing the results, we observe that no discrimination between models can be made on the basis of the χ^2, all models giving an acceptable value.

The results for other values of M_t and M_H can be seen on the contour plots of Figures 12 and 13. The effect of varying the value of α_s in the range $\alpha_s = 0.118$ to 0.128 was found to be small, resulting in a shift in the 95% C.L. contours of less than 0.003 in mixing angle. These results agree with those of an analysis by the L3 collaboration [15].

5.2 Y and Y_L models

The measurements used in the fits are as described in the previous section, apart from the hadronic cross section measurements, which are excluded due to a limitation of the software package available. All the observed cross sections, with the effects of cuts present, are corrected to be Born level values without cuts, using the SM predictions of ZFITTER without Z′ present. An analogous approach to the previous section is used to obtain limits on the additional parameters in these models.

The effects of Z′ on the cross section for the Y and Y_L models were calculated in terms of the parameters $M_{Z'}$, the effective coupling λ^2_{Y,Y_L} and M_Z, for a series of values of M_t, M_H and α_S. The Z mass resulting from the fits is found to deviate from the SM fit result (assuming no Z′) by about 0.014 GeV for the Y_L model. This relatively large deviation compared to the present error on M_Z occurs due to the hadronic cross section data not being used in this fit. For the Y_L model the inclusion of the low energy cross section measurements was found to significantly change the 95% C.L. contour, for example increasing the $M_{Z'}$ limit at $\lambda^2_{Y_L} = 0.3$ from 1210 to 1350 GeV and reducing the $\lambda^2_{Y_L}$ limit at $M_{Z'} = 1200$ GeV from 0.25 to 0.22. There was only a small improvement in the limits for the Y model.

The results are shown in Table 6 and Figure 14. Both these models yield an acceptable χ^2. The 95% C.L. contours show little dependence on the value of M_t.

Model	$E_6(\chi)$	$E_6(\psi)$	$E_6(\eta)$	L-R(1.)	L-R($\sqrt{2}$)	Y	Y_L
χ^2	122.1	121.9	122.1	122.1	121.9	101.0	100.9
ndf	121					104	
$M_{Z'} >$	147.	105.	109.	126.	136.	847.	988.
$M_{Z'}(\theta_{Z'} = 0) >$	147.	105.	109.	126.	139.		
$\theta_{Z'} >$	-0.0070	-0.0075	-0.029	-0.0068	-0.0057		
$\theta_{Z'} <$	0.0078	0.0095	0.029	0.0082	0.0077		

Table 6: 95% confidence-level limits on $M_{Z'}$ and $\theta_{Z'}$ from fits to the predictions of several models, providing the number of degrees of freedom and the χ^2 values obtained; all masses are in GeV and angles in radians.

6 Conclusion

The differential cross sections of final state photons as a function of photon energy and of the angle between the photon and the muon are found to conform to Standard Model expectations.

The cross section measurements below the Z^0, in the energy range 17–86 GeV, for the process $e^+e^- \to \mu^+\mu^-$ agree with Standard Model expectations. There are no statistically significant deviations throughout the energy range. The previous cross section measurement in this energy region made by the OPAL collaboration [19] is repeated with 6 times higher statistics.

These measurements, together with the DELPHI cross section and asymmetry measurements at the LEP energies from 1990 to 1992, are used to determine limits on the Z^0-Z′ gauge boson mixing angle and on the Z′ mass. There is no indication of the existence of a Z′; the mixing angle $\theta_{Z'}$ is consistent with zero for all models. The limits on $\theta_{Z'}$ for the E_6 and L-R models, are consistent with and extend the limits set by L3 [15] and by the indirect studies [14]. In most cases the 95% confidence level limits on $\theta_{Z'}$ are almost symmetric about zero with $|\theta_{Z'}| < 0.009$. The mass limits for the Y and Y_L models are considerably improved over the existing limit of $M_{Z'} > 250$ GeV [25] to $M_{Z'} > 847$ and 988 GeV respectively.

Acknowledgements

We are greatly indebted to our technical collaborators and to the funding agencies for their support in building and operating the DELPHI detector, and to the members of the CERN-SL Division for the excellent performance of the LEP collider.

Also we would like to thank Sabine Riemann for providing us with the ZEFIT program and invaluable advice on its use.

References

[1] M. Sakuda, "New Results from TRISTAN Experiments", preprint KEK 93-124, Sep 1993.

[2] ALEPH Collaboration, D. Decamp et al., Z. Phys. **C53** (1992) 1.

[3] DELPHI Collaboration, P. Abreu et al., Nucl. Phys. **B367** (1991) 511.
DELPHI Collaboration, P. Abreu et al., Nucl. Phys. **B417** (1994) 3.
DELPHI Collaboration, P. Abreu et al., "Improved measurements of cross sections and asymmetries at the Z^0 resonance", preprint CERN PPE 94-31, to be published in Nucl. Phys.**B**

[4] L3 Collaboration, B. Adeva et al., Z. Phys. **C51** (1991) 179.

[5] OPAL Collaboration, G. Alexander et al., Z. Phys. **C52** (1991) 175.

[6] Z Physics at LEP 1, edited by G. Altarelli, R.Kleiss and C.Verzegnassi, CERN 89-08 (1989).

[7] D.C. Kennedy et al., Nucl. Phys **B321** (1989) 83;
D.C. Kennedy and B.W. Lynn, Nucl. Phys **B322** (1989) 1.

[8] ZFITTER is a package, produced by the Dubna-Zeuthen radiative correction group, for fitting Z^0 data in either a quasi-model independent way or within the MSM.
D.Bardin et al.,"ZFITTER: An Analytical Program for Fermion Pair Production in e^+e^- Annihilation", preprint CERN-TH 6443/92 (1992); Phys. Lett. **B229** (1989) 405; Z. Phys.**C44** (1989) 493; Nucl. Phys. **B351** (1991) 1; Comp. Phys. Comm. **59** (1990) 303; Berlin-Zeuthen preprint PHE89-19(1989).

[9] F.Berends, "Z line shape", in [6] p. 89.

[10] J.E. Campagne and R. Zitoun, Z. Phys. **C43** (1989) 469; and Proc. of the Brighton Workshop on Radiative Corrections, Sussex, July 1989.

[11] For reviews and further references see:
"Unity of Forces in the Universe", A.Zee, World Scientific, Singapore, 1982;
"Supersymmetry", ed. S.Ferrara, North Holland, Amsterdam and World Scientific, Singapore, 1987;
"Superstrings", ed. J.H.Schwarz, World Scientific, Singapore, 1985.
See also: M.Veltman, Acta Phys. Pol. **B8** (1977) 475;
M.S.Chanowitz and M.K.Gaillard, Nucl. Phys. **B261** (1985) 379;
R.Casalbuoni, P.Chiappetta, D.Dominici, F.Feruglio and R.Gatto, Nucl. Phys. **B310** (1988) 181;
J.Ellis, K.Enqvist, D.V.Nanopoulos and F.Zwirner, Nucl. Phys. **B276** (1986) 14;
F.Zwirner, Int. Journ. of Mod. Phys. **A3** (1988) 49;
J.C.Pati and A.Salam, Phys. Rev. **D10** (1974) 275;
J.Layssac, F.M.Renard and C.Verzegnassi, Z.Phys. **C53** (1992) 97;
A.A.Pankov and C.Verzegnassi, Phys. Lett. **B233** (1989) 259.

[12] J.Layssac, F.M.Renard and C.Verzegnassi, Z.Phys. **C53** (1992) 97;
U.Baur, M.Linder and K.H.Schwarzer, Nucl. Phys. **B291** (1987) 1;
M.Kuroda, F.M.Renard and D.Schildknecht, Phys. Lett. **B183** (1987) 366.
[13] CDF Collaboration, F. Abe et al., Phys. Rev. Lett. **68** (1992) 1463.
[14] G.Altarelli, Phys. Lett., **B318** (1993) 139;
P.B.Renton, Z.Phys. **C56** (1992) 355;
P.Langacker and M.Luo, Phys. Rev. **D45** (1992) 278;
E.Nardi, E.Roulet and D.Tommasini, Phys. Rev. **D46** (1992) 3040;
F. del Aguila, W.Hollik, J.M.Moreno and M.Quiros, Nucl. Phys. **B372** (1992) 1;
M.C.Gonzalez-Garcia and J.W.F.Valle, Phys. Lett. **B259** (1991) 365;
[15] L3 Collaboration, B. Adeva et al., Phys. Lett. **B306** (1993) 187.
[16] A.Leike, S. Riemann and T. Riemann, Munich University preprint LMU-91/06,
and FORTRAN program ZEFIT; and Phys. Lett. **B291** (1992) 187.
[17] S.S.Gershtein, A.A.Likhoded, A.A.Pankov and O.P.Yushchenko, Z. Phys. **C56** (1992) 279;
A.A.Likhoded, A.A.Pankov and O.P.Yushchenko, Int. J. Mod. Phys. **A7** (1992) 5537;
[18] DELPHI Collaboration, P. Aarnio et al., Nucl. Instr. & Meth. **A303** (1991) 233.
[19] OPAL Collaboration, D.P.Acton et al., Phys. Lett. **B273** (1991) 338.
[20] W.T.Eadie et al. Statistical Methods in Experimental Physics, p.166;
N.J.Kjaer, private communication.
[21] Z.Was and S.Jadach, Phys. Rev. **D41** (1990) 1425.
[22] P.Langacker, R.W.Robinett and J.L.Rosner, Phys. Rev. **D30** (1984) 1470;
D.London and J.L.Rosner, Phys. Rev. **D34** (1986) 1530.
[23] J.C.Pati and A.Salam, Phys. Rev. **D10** (1974) 275;
R.N.Mohapatra and J.C.Pati, Phys. Rev. **D11** (1975) 566.
[24] DELPHI Collaboration, P. Abreu et al., Z. Phys. **C59** (1993) 21.
[25] M.Kuroda, D.Schildknecht and K.H.Schwarzer, Nucl. Phys. **B261** (1985) 432.

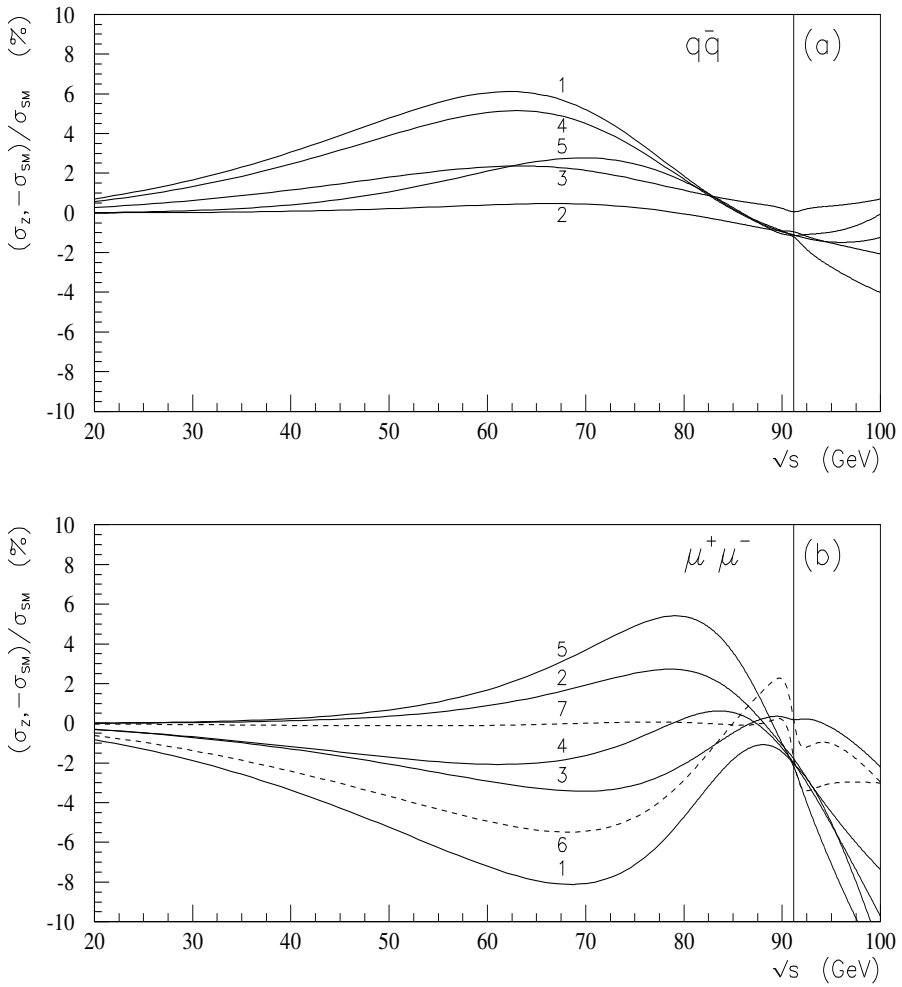

Figure 1: Fractional deviation: $(\sigma_{Z'} - \sigma_{SM})/\sigma_{SM}$, of (a) hadronic and (b) muon-pair cross sections as functions of energy for several Z′ models. The numbers refer to the models: 1 = $E_6(\chi)$, 2 = $E_6(\psi)$, 3 = $E_6(\eta)$, 4 = L-R($\sqrt{2/3}$), 5 = L-R(1.), 6 = Y, 7 = Y_L. For the E_6 and L-R models $M_{Z'} = 150$ GeV, $\theta_{Z'} = 0.01$ radians and for the Y and Y_L models $M_{Z'} = 650$ GeV, $\lambda^2_{Y,Y_L} = 0.1$. The vertical line indicates the energy $\sqrt{s} = M_Z$.

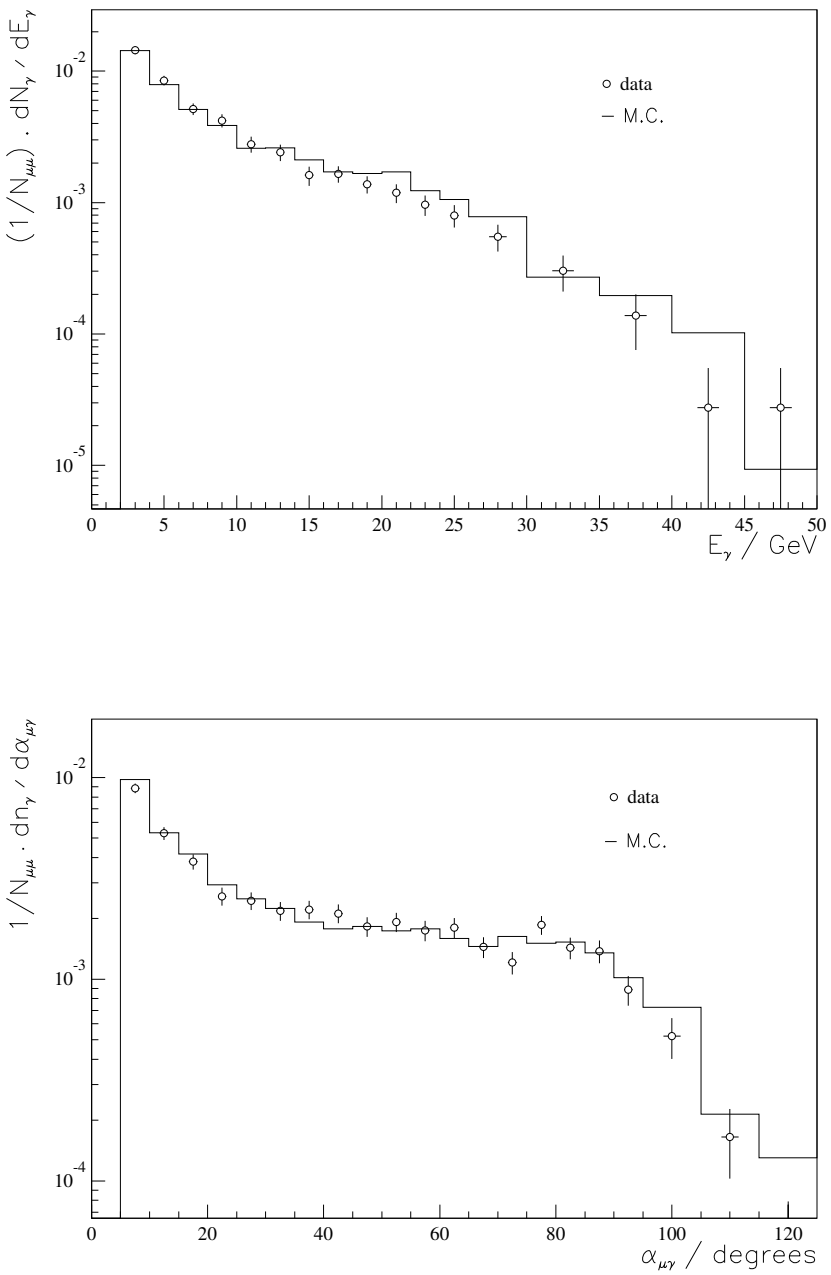

Figure 2: Corrected distributions for isolated photons of energy E_γ and angle $\alpha_{\mu\gamma}$ to the nearer muon. The errors shown are statistical only. The solid line shows the DYMU3 prediction with a factor of two higher statistics.

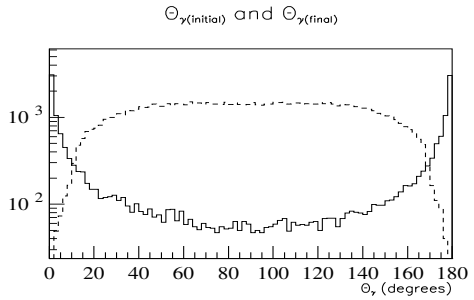

Figure 3: The generator level θ_γ of the highest energy photon in events classed as ISR (solid line) and FSR (dashed line), as defined in text; obtained from $\sim 0.7 \cdot 10^6$ generated muon-pair events.

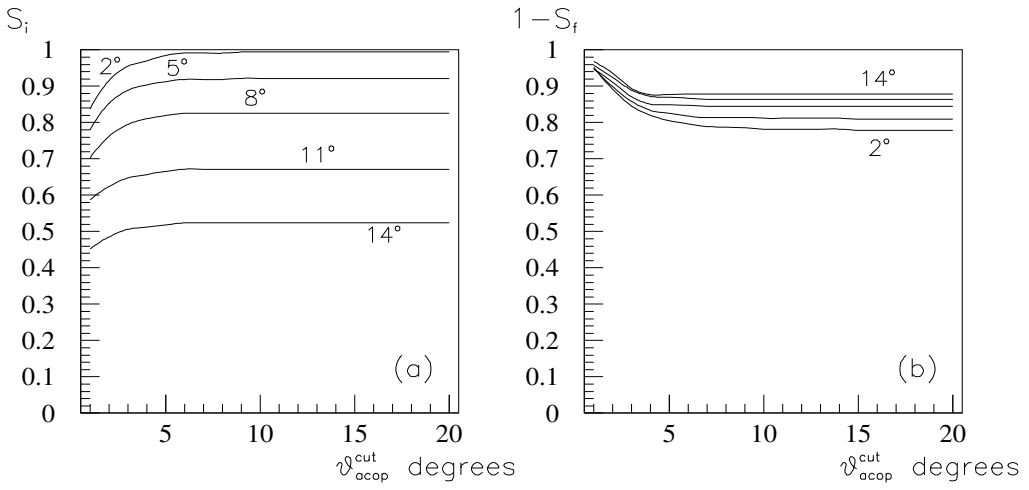

Figure 4: Selection **A**: (a) efficiency S_i and (b) purity $1-S_f$, for the mass interval $73 < M_{\mu\mu} < 80$ GeV with angular cuts $\theta_{acop} < \theta^{cut}_{acop}$ and $\theta_{acol} > \theta^{cut}_{acol}$, as a function of θ^{cut}_{acop} for $\theta^{cut}_{acol} = 2, 5, 8, 11, 14°$, with an additional cut excluding photons of energy greater than 3 GeV within the acceptance of the electromagnetic calorimeters.

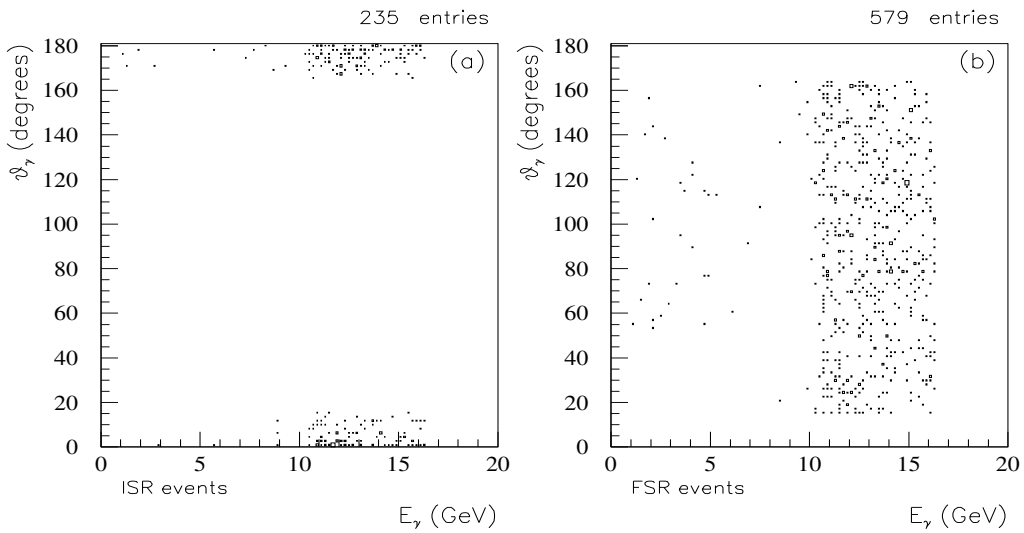

Figure 5: θ_γ vs E_γ distributions from $0.886 \cdot 10^6$ generated muon-pair events, classified as (a) ISR and (b) FSR after the cuts : $\theta_{acol} > 7°$, $\theta_{acop} < 4°$ for the mass interval $73 < \mathrm{M}_{\mu\mu} < 80$ GeV.

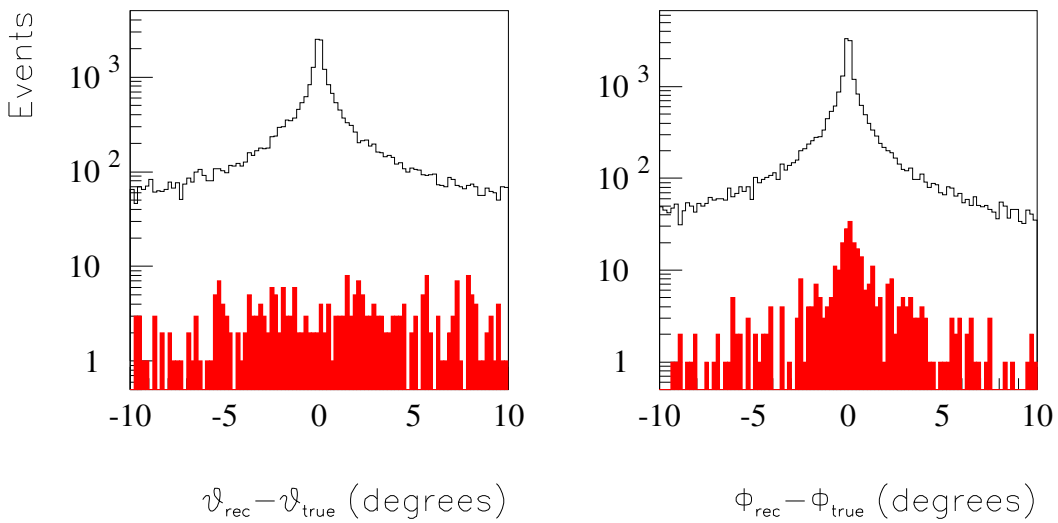

Figure 6: The reconstruction performance is demonstrated by comparison of the reconstructed and simulated photon angles, for $0.15 \cdot 10^6$ simulated muon-pair events. For events with more than one photon, the comparison is made with the most energetic photon. The shaded histogram indicates events with two photons, each of energy greater than 1 GeV.

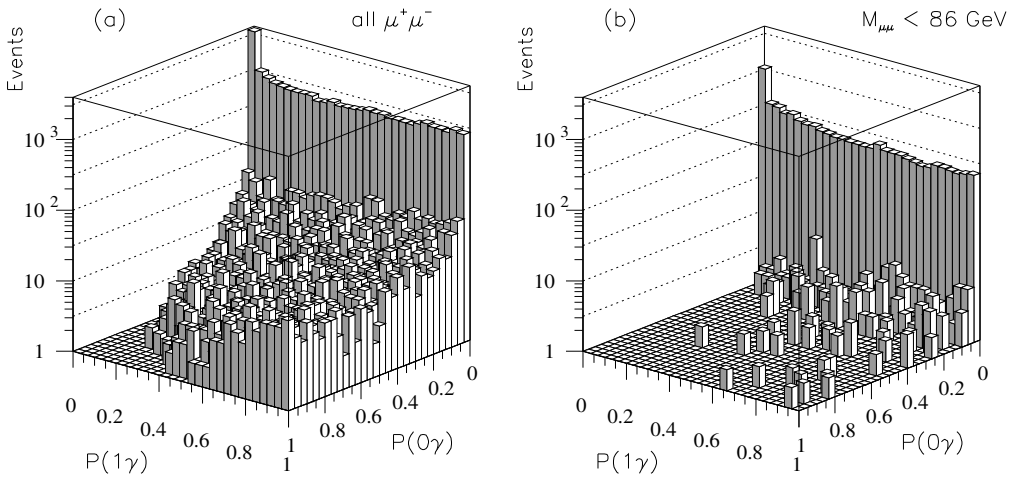

Figure 7: $P(1\gamma)$ and $P(0\gamma)$ are the χ^2 probabilities from fits assuming respectively that only 1 photon is produced and that no photons are produced. Plot (a) is obtained from the full data sample of $\mu^+\mu^-$ events and plot (b) from events in the invariant mass range $M_{\mu\mu} < 86$ GeV.

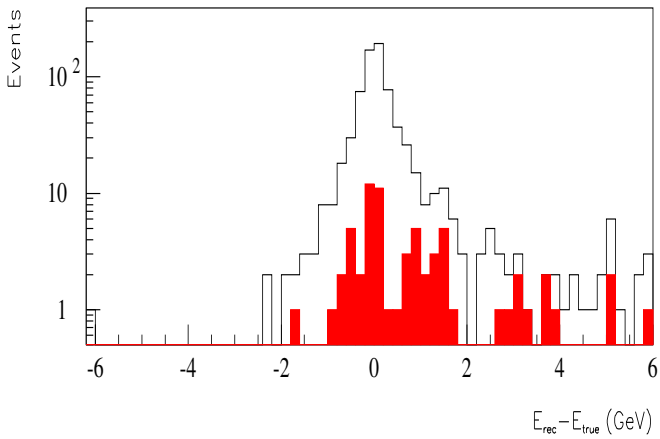

Figure 8: The reconstruction of the unseen photon, in events selected as ISR by method B and with invariant mass $M_{\mu\mu} < 86$ GeV, is demonstrated by comparison of the photon energy E_γ reconstructed in a simulated event and the true energy. In events with more than one photon the comparison is made with the most energetic photon. The shaded histogram indicates those events with two photons, each of energy greater than 1 GeV.

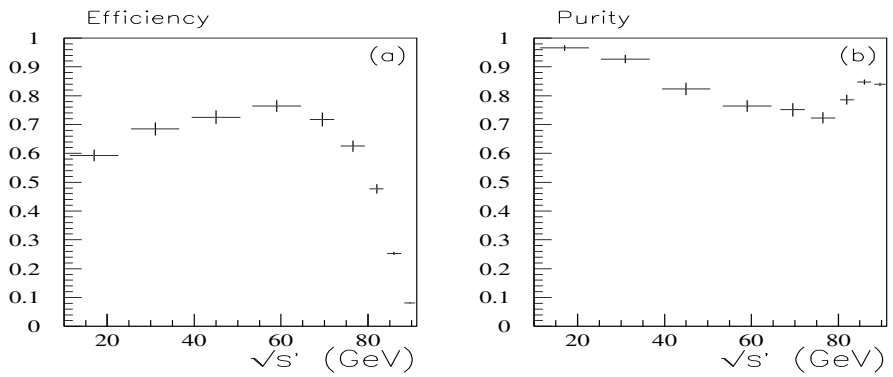

Figure 9: (a) ISR efficiency and (b) purity, as a function of effective energy $\sqrt{s'}$, from simulation, as defined in the text, for selection **B**

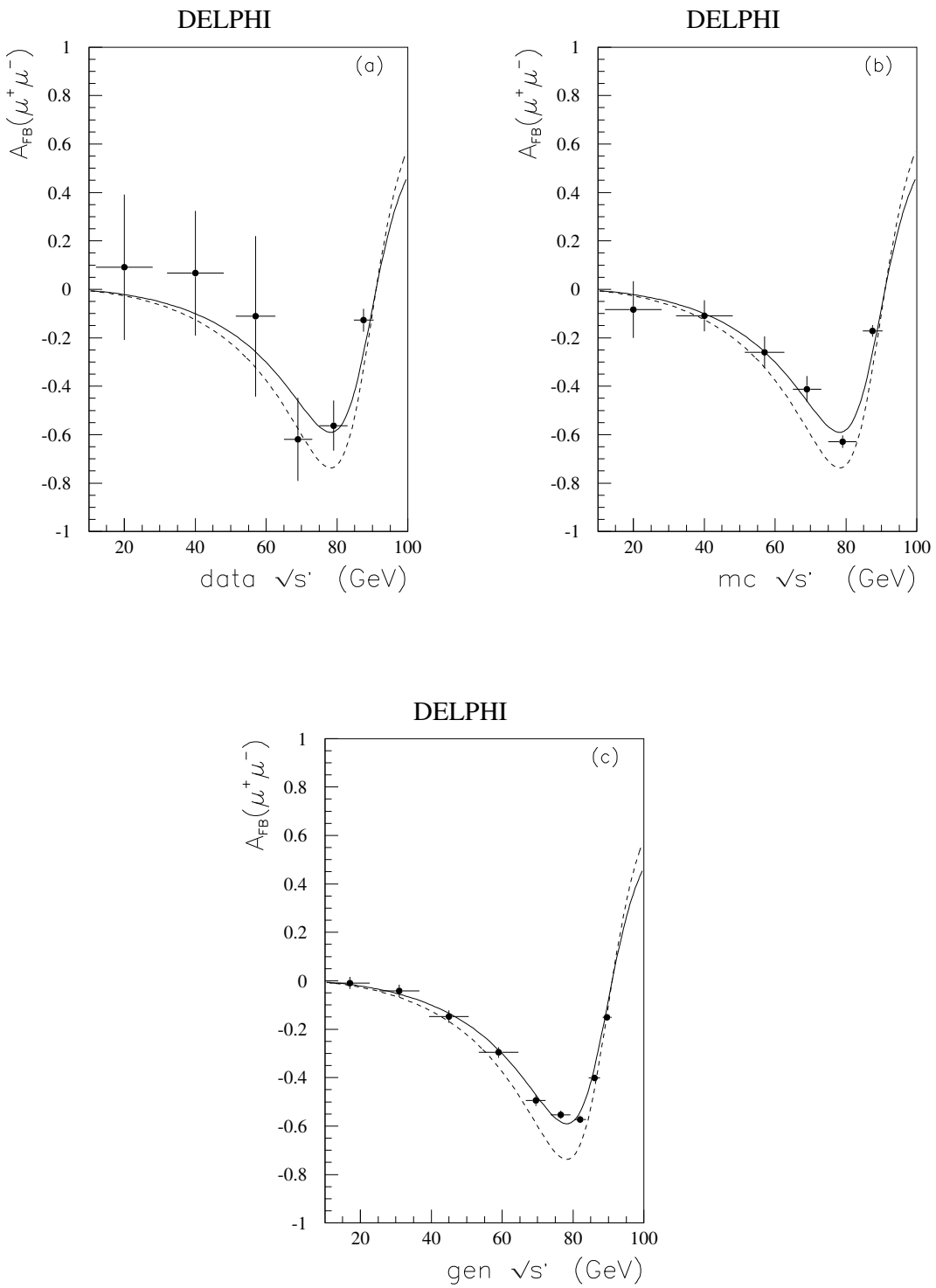

Figure 10: Asymmetry in bins of effective energy from selection **B**, for (a) data, (b) full simulation and (c) DYMU3 generated events after momentum smearing. The dashed curve is the Born approximation asymmetry, the solid curve corresponds to 80% of the Born approximation asymmetry, as explained in the text.

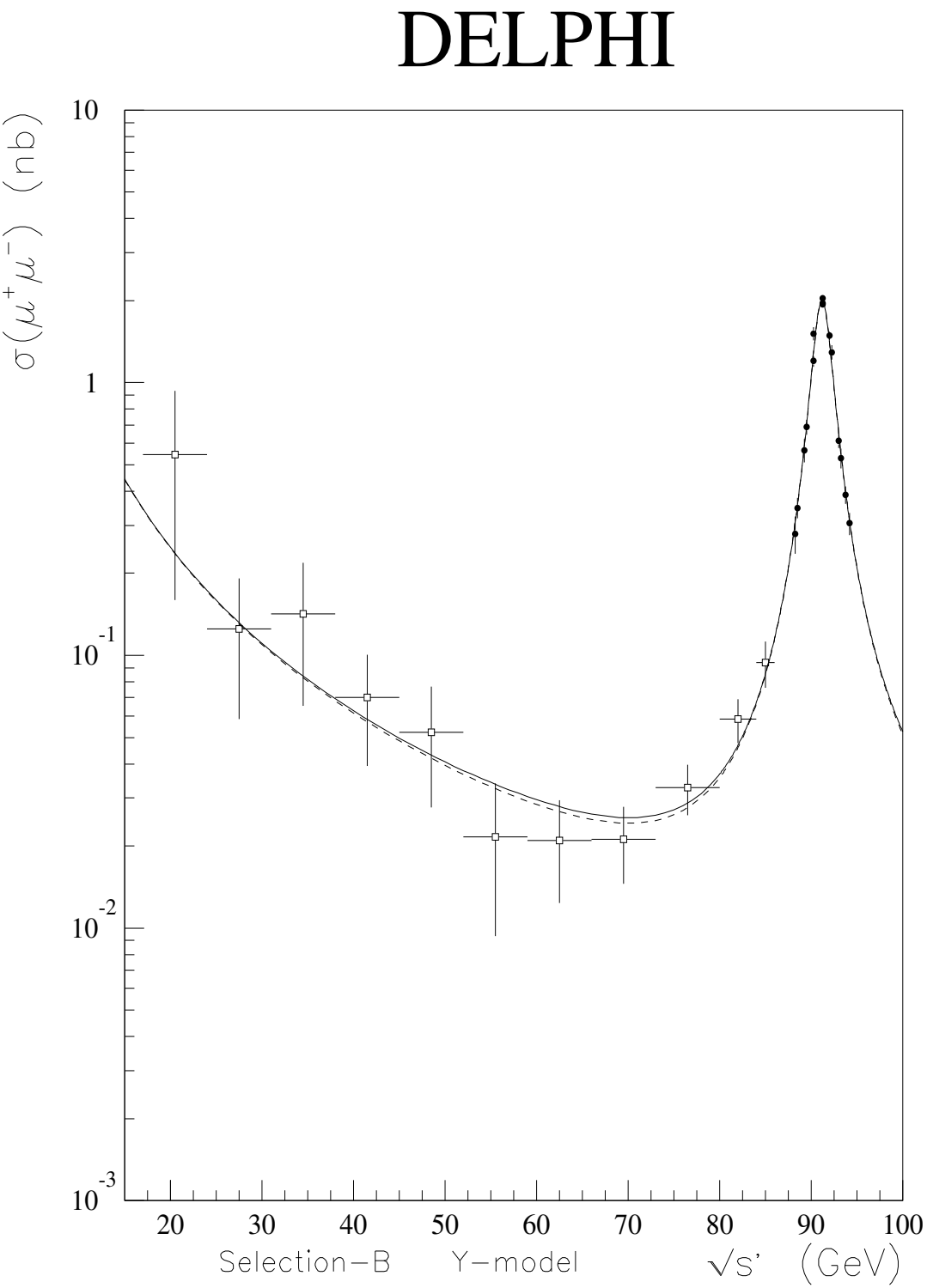

Figure 11: Cross section for $e^+e^- \to \mu^+\mu^-$ with selection **B**. The solid curve is the Born cross section in the SM and the dashed one is the cross section with the fitted values of $M_{Z'}$ and $\lambda_{Z'}$, using model Y. The solid dots are the on peak cross section measurements corrected to Born level and the open dots are the below peak measurements.

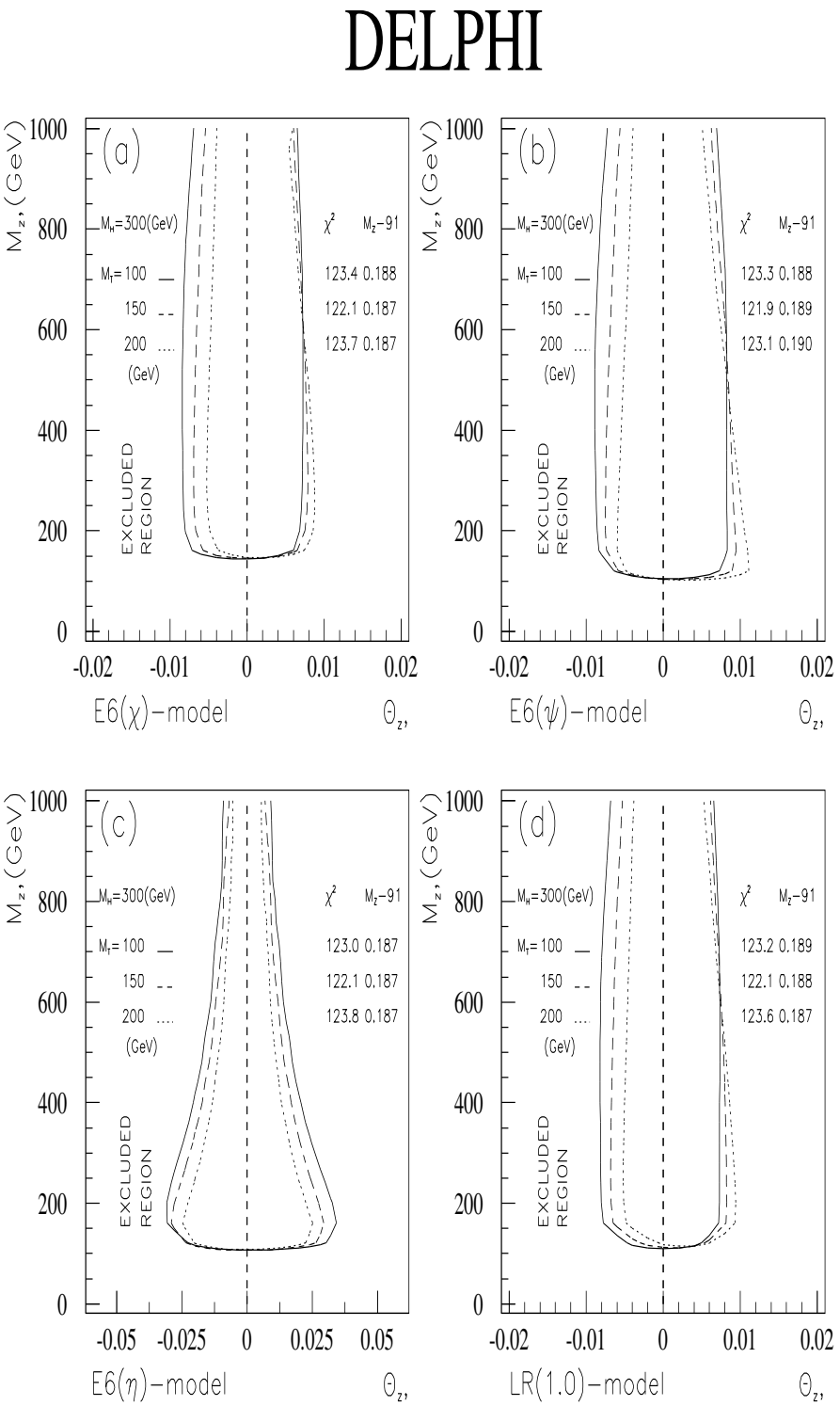

Figure 12: Curves corresponding to 95% confidence limits, dividing the $M_{Z'} - \theta_{Z'}$ plane into allowed and excluded regions; for $M_H = 300$ GeV and $M_t = 100, 150, 200$ GeV; all masses are in GeV and angles in radians.

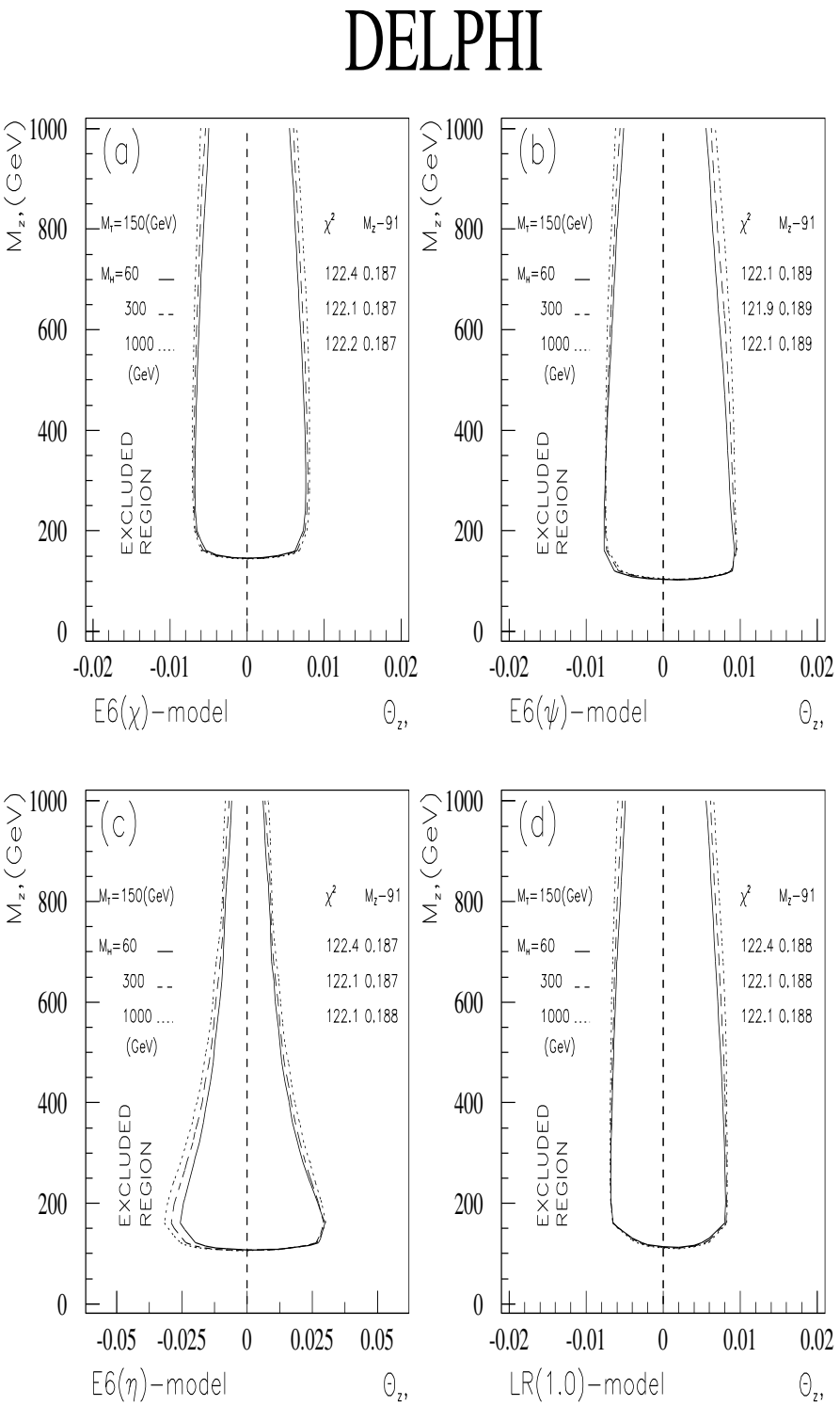

Figure 13: Curves corresponding to 95% confidence limits, dividing the $M_{Z'} - \theta_{Z'}$ plane into allowed and excluded regions; for $M_t = 150$ GeV and $M_H = 60, 300, 1000$ GeV; all masses are in GeV and angles in radians.

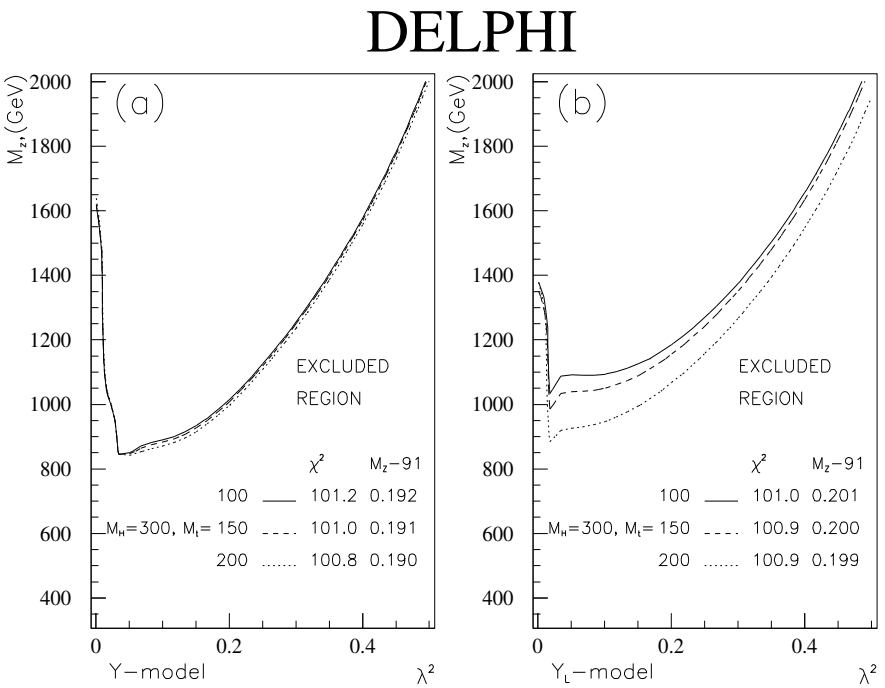

Figure 14: Curves corresponding to 95% confidence limits, dividing the $M_{Z'} - \lambda^2_{Y,Y_L}$ plane into allowed and excluded regions; for (a) the Y model and (b) the Y_L model, with $M_H = 300$ GeV and $M_t = 100, 150, 200$ GeV; all masses are in GeV.